

This is the peer reviewed version of the following article:

Microstructure-based thermo-mechanical modelling of thermal spray coatings / Bolelli, Giovanni; Candeli, Alessia; Koivuluoto, Heli; Lusvarghi, Luca; Manfredini, Tiziano; Vuoristo, Petri. - In: MATERIALS & DESIGN. - ISSN 1873-4197. - ELETTRONICO. - 73:(2015), pp. 20-34. [10.1016/j.matdes.2015.02.014]

Terms of use:

The terms and conditions for the reuse of this version of the manuscript are specified in the publishing policy. For all terms of use and more information see the publisher's website.

19/12/2025 04:19

Accepted Manuscript

Microstructure-based thermo-mechanical modelling of thermal spray coatings

Giovanni Bolelli, Alessia Candeli, Heli Koivuluoto, Luca Lusvarghi, Tiziano Manfredini, Petri Vuoristo

PII: S0261-3069(15)00060-6

DOI: <http://dx.doi.org/10.1016/j.matdes.2015.02.014>

Reference: JMAD 7101

To appear in: *Materials and Design*

Received Date: 15 November 2014

Accepted Date: 18 February 2015



Please cite this article as: Bolelli, G., Candeli, A., Koivuluoto, H., Lusvarghi, L., Manfredini, T., Vuoristo, P., Microstructure-based thermo-mechanical modelling of thermal spray coatings, *Materials and Design* (2015), doi: <http://dx.doi.org/10.1016/j.matdes.2015.02.014>

This is a PDF file of an unedited manuscript that has been accepted for publication. As a service to our customers we are providing this early version of the manuscript. The manuscript will undergo copyediting, typesetting, and review of the resulting proof before it is published in its final form. Please note that during the production process errors may be discovered which could affect the content, and all legal disclaimers that apply to the journal pertain.

Microstructure-based thermo-mechanical modelling of thermal spray coatings

Giovanni Bolelli^{1,*}, Alessia Candeli¹, Heli Koivuluoto², Luca Lusvarghi¹, Tiziano Manfredini¹,
Petri Vuoristo²

¹ Department of Engineering “Enzo Ferrari”, University of Modena and Reggio Emilia, Via Pietro
Vivarelli 10/1, I-41125 Modena (MO), Italy

² Department of Materials Science, Tampere University of Technology, Korkeakoulunkatu 6, FI-
33720 Tampere, Finland

* Corresponding author:

Tel.: 0039 0592056233; Fax: 0039 0592056243; e-mail: giovanni.bolelli@unimore.it

Abstract

This paper demonstrates how microstructure-based finite element (FE) modelling can be used to interpret and predict the thermo-mechanical behaviour of thermal spray coatings. Validation is obtained by comparison to experimental and/or literature data.

Finite element meshes are therefore constructed on SEM micrographs of high velocity oxygen-fuel (HVOF)-sprayed hardmetals (WC-CoCr, WC-FeCrAl) and plasma-sprayed Cr₂O₃, employed as case studies. Uniaxial tensile tests simulated on high-magnification micrographs return micro-scale elastic modulus values in good agreement with depth-sensing Berkovich micro-indentation measurements. At the macro-scale, simulated and experimental three-point bending tests are also in

good agreement, capturing the typical size-dependency of the mechanical properties of these materials. The models also predict the progressive stiffening of porous plasma-sprayed Cr_2O_3 due to crack closure under compressive loading, in agreement with literature reports.

Refined models of hardmetal coatings, accounting for plastic behaviours and failure stresses, predict crack initiation locations as observed by indentation tests, highlighting the relevance of stress concentrations around microstructural defects (e.g. oxide inclusions).

Sliding contact simulations between a hardmetal surface and a small spherical asperity reproduce the fundamental processes in tribological pairings. The experimentally observed “wavy” morphologies of actual wear surfaces are therefore explained by a mechanism of micro-scale plastic flow and matrix extrusion.

Key-words: Thermal spray; Coatings; Finite element simulation; Microstructure based model; Elastic properties; Contact simulation.

1. Introduction

In many areas of industrial technology, coatings play an important role in conferring improved functional properties to machine parts, and the need has continuously been arising to integrate coatings as *a priori* constituents of components design (as clearly laid out e.g. in official reports and strategic visions [1,2]). This requires full consideration of the coating in stress-strain analyses of a structural component; therefore, all of the thermo-mechanical properties of the coating (e.g. tensor of elasticity, thermal conductivity, etc.) must be known in detail [2]. Measuring these properties is often not an easy task, due to the experimental difficulties in applying conventional macro-mechanical testing methods. For instance, the conventional uniaxial tensile testing according to ISO 6892-1:2009 [3], routinely applied to bulk metals, is hardly applicable as getting a suitable sample out of a coating is usually impractical. Manufacturing free-standing coatings or machining them without inducing undesirable damage is a complex task. Even when this was possible, the coating, in most cases, would have to be manufactured to a greater thickness than in actual applications, which may significantly affect its actual characteristics.

Ceramic and hardmetal coatings manufactured by thermal spray techniques are of particular relevance in this respect. On the one hand, they have gained widespread use for wear protection of structural and functional parts e.g. in the pulp and paper industry, in the steelmaking sector, in pumps and hydraulic machinery, etc. [4]. On the other hand, quantitative values of their thermo-mechanical properties are particularly hard to obtain, as they are usually different from those of corresponding bulk materials. The properties of thermally sprayed materials are indeed critically affected by microstructural features such as lamellar boundaries, pores, oxide inclusions, etc. [5,6], and the latter depend on the specific deposition conditions (including the specific type of process, the operating parameters, the characteristics of the feedstock powder, etc.) [4,6], so that coatings with nominally identical composition may differ significantly in practice.

The complete characterisation of each individual thermal spray coating, accounting for its microstructural specificities, would however become a very burdensome task. This would be remarkably lessened if validated numerical models, capable of predicting the thermo-mechanical properties of materials starting from their microstructure, were available. Moreover, thermo-mechanical simulations of materials at the microscale, revealing stress and strain distributions across microstructural features [7,8], would also allow the identification of critical features which would be overlooked in a purely macro-scale mechanical analysis where materials are assumed to be homogeneous.

Microstructure-based computational techniques do exist in the literature [9] and, in recent years, they have been very actively explored in order to get new insights into the thermo-mechanical behaviour of various bulk materials. Examples include the interpretation of the microscale phenomena underlying the plasticity and damage of multiphase metals, such as $\alpha+\beta$ Ti alloys or dual-phase (ferrite+pearlite or ferrite+martensite) steels [10-14], or the analysis of stress distribution and crack formation mechanisms in different types of composites [15-19]. Their use for the simulation, interpretation and prediction of the properties of thermal spray coatings, however, is still not widespread. A few of the existing papers analysed schematic reconstructions of the defect structure of thermal spray coatings using standard finite element software [7,8,20-23]. Others employed scanning electron microscopy (SEM) or (more rarely) micro-tomography reconstructions of actual coating microstructures [5,7,24-40], analysing them either by the finite difference method [24,35] or, more frequently, by the finite element one. Most of these papers deal with thermal spray ceramic coatings, whereas hardmetal coatings have more seldom been considered [7,40]. In particular, the open source finite-element software OOF (Object-Oriented Finite Element Software) program [9] and its updated version OOF2 [41] were often used [5,7,24,26,28,29,31,33-35,37-39]. These codes create bi-dimensional finite element meshes on images, such as optical and SEM micrographs. Each constituent of the microstructure of a material can be assigned its intrinsic

properties and “virtual experiments” (e.g. simulated tensile or heat conduction tests) can be performed by applying various thermo-mechanical loads as boundary conditions [7,9,39] in order to extract overall, macro-scale material properties.

The potential usefulness of these methods calls for further validation against experimental data, in view of their eventual predictive application for research, development and industrial design purposes. Moreover, there are large, yet unexplored potentials in the coupling of microstructure-based meshing techniques to standard finite element software. This would allow the simulation of more complex phenomena, e.g. micro-scale contacts between fine asperities and the actual microstructural features of the coatings. This, however, has very seldom been done in the available literature [8,29,40].

The goal of the present paper is therefore to provide an overview of the modelling potentials that are enabled by the use of microstructure-based finite element software (such as OOF2) coupled to standard, commercial software (ABAQUS), and to validate the models by comparing the results to experimental measurements and to available literature data.

Hardmetal coatings, including a WC-10%Co-4%Cr coating deposited by a liquid-fuelled High Velocity Oxygen-Fuel (HVOF) torch and two WC-15%FeCrAl coatings deposited by liquid- and gas-fuelled HVOF spraying (respectively), and one Cr₂O₃ coating obtained by atmospheric plasma spraying (APS) were considered in this study. Models were implemented in order to simulate some of the most peculiar features of these materials:

- Starting from SEM micrographs taken at different magnifications, the elastic properties were obtained at different length scales to capture the typical size-dependent behaviour of the response of thermal spray coatings [42,43]. Numerical results were compared to experimental measurements of the elastic modulus performed at the micro-scale (by depth-sensing micro-

indentation on polished cross-sections and top surfaces) and at the macro-scale (by three-point bending tests).

- Microstructure-based heat conduction simulations were also performed to extract thermal conductivity values for comparison against literature data [44,45].
- The elastic modulus of APS ceramic coatings is known to change when tested in tension or in compression, because of the opening or closure of micro-cracks, respectively [46-49]. By exploiting the possibility to enforce self-contact controls in standard finite element programs, microstructure-based simulations can be run on APS Cr_2O_3 under tensile or compressive conditions, capturing the effect of crack closure on the actual, macro-scale elastic modulus.
- The contact between hard surfaces in sliding conditions is often localised on asperities, the micrometre-scale radius of which [50] is comparable to the size of microstructural features of coatings. Macro-scale models neglecting the latter may therefore lead to significant errors, which can be overcome by running standard finite element software on microstructure-based meshes.

2. Materials and experimental methods

2.1 Sample manufacturing and microstructural analysis

Three HVOF-sprayed hardmetals were considered in this study: a WC – 10wt.%Co – 4wt.%Cr coating, deposited by a kerosene-fuelled JP5000 HVOF torch (Praxair-Tafa, Concord, NH, USA), and two WC – 15wt.%FeCrAl coatings, sprayed using a JP5000 torch and a gas-fuelled Diamond Jet 2700 HVOF torch (Oerlikon-Metco, Wohlen, Switzerland) respectively. The coatings were sprayed onto grit-blasted plain carbon steel plates, using deposition conditions detailed in a previous publication [51]. The thickness of the three coatings is comprised between 150 μm and 250 μm .

Furthermore, an APS Cr_2O_3 coating was manufactured at an industrial facility onto plain carbon steel disks of 32 mm diameter x 5 mm thickness, using a single-cathode DC plasma torch.

The main thermo-mechanical properties of these samples are summarised in Table I.

Cross-sectional samples of hardmetal coatings, obtained by metallographic cutting, were hot-mounted in phenol resin, ground using diamond papers (up to 2000 mesh) and polished using diamond slurries (6 μm and 3 μm) and colloidal silica suspension. Two types of micrographs were acquired by scanning electron microscopy (SEM: XL30, FEI, Eindhoven, The Netherlands) for modelling purposes:

- 1) High definition (1936 x 1452 pixels) backscattered electron micrographs at 10000x magnification (6 for each coating), covering a field of 12.4 μm length x 9.3 μm height, in order capture small-scale microstructural details, including the actual size, shape and distribution of WC particles and of oxide inclusions;
- 2) Backscattered electron micrographs at low magnification (200x): sequences of 4 consecutive micrographs were acquired, in order to reconstruct an overall material length of approximately 2.3 mm, accounting for meso-scale features such as the distribution of larger pores.

The cross-section of APS Cr_2O_3 , obtained by cutting, cold-mounting in epoxy resin and polished as described above, was imaged by SEM in backscattered electron mode at 2000x magnifications. This magnification was chosen based on preliminary tests as it provides the best compromise between the need to capture fine microstructural details (e.g. fine pores and microcracks) and that of having a material portion representative of the overall characteristics of the sample (“representative volume element” – RVE). High-resolution (2576 x 1936 pixels) micrographs were acquired, covering a field of 61.98 x 46.50 μm size.

Some additional microstructural observations were performed on fracture surfaces, obtained by cutting small bar-shaped probes (through a semi-automatic metallographic cutting machine) from the coated samples and by breaking them after immersion in liquid nitrogen for at least 1 min.

2.2 Mechanical characterisation

As recalled in the Introduction, it is well known that thermal spray coatings exhibit a scaling behaviour in their mechanical properties, which are increasingly affected by pores and defects as the tested length scale increases [42,43].

At the micro-scale, the elastic modulus was characterised by depth-sensing Berkovich micro-indentation (Micro-Combi tester, Anton-Paar, Peseux, Switzerland), using a maximum applied load of 3 N, a loading-unloading rate of 4.5 N/min and a holding time at maximum load of 15 s. Thermal spray coatings are known to be transversely isotropic materials: their mechanical properties often differ along the spray direction (i.e. the direction perpendicular to the coating/substrate interface) and in the in-plane directions (i.e. on a plane parallel to the coating/substrate interface) [61-64]. The micro-scale elastic modulus of hardmetal coatings was therefore measured both along the spray direction, by indenting into their cross-section, and in the in-plane direction, by indenting into their top surface (polished according to the same procedure outlined previously), in accordance with the literature [61-64]. In the case of APS Cr_2O_3 , indentations were performed on the cross-section only, because of the risk of pull-out artefacts while grinding and polishing the top surface of an APS ceramic coating, not embedded in resin; the elastic modulus was therefore measured along the spray direction only.

Twenty indentations were performed on each sample; hardness and elastic modulus were computed using the Oliver-Pharr method [65], in accordance with the relevant standard [66,67]. The Poisson's

ratio of hardmetal was assumed to be 0.30 and that of Cr_2O_3 was estimated to be 0.27, which corresponds to the value for bulk Cr_2O_3 [60].

At the macro-scale, dynamic three-point bending tests were performed on free-standing beam-shaped WC-CoCr samples of 5 mm width and 30 mm length, extracted from the coated plates by metallographic cutting, grinding and eventual acid etching. The tests were carried out using a Dynamical Mechanical Analyser (DMA: Q800, TA Instruments, New Castle, DE, USA) with an oscillation frequency of 1 Hz and an amplitude of 25 μm . The storage modulus (E') was compared to the results of simulated static three-point bending tests (Section 3).

Dry sliding wear tests were also performed on the polished top surface of WC-CoCr in ball-on-disk configuration, against a 6 mm-diameter Al_2O_3 counterpart. Full details of the experimental procedure and of the results are given in [51]; in this study, the detailed morphology of the worn surface was employed as a term of comparison for the micro-scale asperity contact simulations (Section 3).

3. Finite element simulation procedures

Microstructure-based meshing was performed using the OOF2 software [41] version 2.1.6. SEM micrographs (such as the one shown in Fig. 1A) were preliminarily treated using open source image processing and analysis software (ImageJ and The Gimp), in order to isolate the various constituent phases based on their respective greyscale contrast levels (Fig. 1B).

Various simulations were then run on the processed micrographs:

- 1) On the high-magnification (10000x) cross-sectional micrographs of HVOF-sprayed hardmetals (such as the one shown in Fig. 1: see Section 2.1), simulated tensile tests were

performed along the x direction (i.e. the in-plane direction, parallel to the coating/substrate interface) and along the y direction (i.e. the spray direction), Fig. 2.

Mesheres of mixed 8-node quadrangular elements (Fig. 2A) or of mixed 8-node quadrangles and 6-node triangles (Fig. 2B) were built. Mesheres were refined until the homogeneity index, indicating the ability of the mesh to reproduce the microstructure [41], was ≥ 0.96 . Mesheres consisted of 25000 – 30000 elements. All microstructural constituents were considered as isotropic and purely elastic materials, with properties listed in Table I.

Computations were performed using both the built-in finite element solver of OOF2 and the commercial finite element solver ABAQUS version 6.12-3 (Simulia – Dassault Systemes, Waltham, MA, USA). In the latter case, meshes were exported from OOF2 in Abaqus-compatible format. For y -direction tensile test simulation, the y displacements at the bottom and top boundaries were set to zero and to $1.86 \cdot 10^{-2} \mu\text{m}$, respectively (corresponding to an overall strain $\varepsilon_y = 2\%$; Fig. 2A); moreover, a constant x displacement was imposed along the left and right boundaries, to account for the constraint coming from the surrounding material in an actual coating. For the same reason, plane strain was assumed.

The overall elastic modulus of the material along the y direction (E_y) was computed from the numerical results using equation (1), which is equivalent to the approach previously employed in [39]:

$$E_y = \frac{\widehat{\sigma}_y}{\varepsilon_y} = \frac{\frac{1}{L_x} \int_0^{L_x} \sigma_y(x, L_y) dx}{\Delta L_y / L_y} \quad (1)$$

Where:

$\widehat{\sigma}_y$ = average normal stress along the y direction across the top boundary;

ε_y = deformation along the y direction;

L_x, L_y = dimensions of the computational domain along the x, y directions (respectively);

ΔL_y = prescribed y displacement of the top boundary;

x = coordinate along the x direction;

$\sigma_y(x, L_y)$ = normal stress component along the y direction at coordinates (x, L_y) , i.e. along the top boundary of the computational domain.

Analogous procedures were employed to determine the elastic modulus E_x along the x direction, by fixing the left boundary and prescribing an x -displacement corresponding to a deformation $\epsilon_x = 2\%$ at the right boundary. Equation (1) was changed accordingly to extract E_x .

Additional simulations were performed on some of the micrographs by imposing different displacements along both x and y directions, corresponding to overall strains of 0.5%, 1%, 1.3%, 1.5%, in order to check that the method would correctly return a linear elastic behaviour and constant elastic moduli E_x and E_y , independent of the imposed displacement.

2) On the high-magnification (2000x) cross-sectional micrographs of APS Cr_2O_3 (example of an original micrograph in Fig. 3A and processed micrograph in Fig. 3B), analogous simulated uniaxial tests were performed along the x and y directions, again using the Abaqus finite element solver on microstructure-based meshes generated by OOF2 and exported in Abaqus-compatible format. The elastic properties of bulk Cr_2O_3 , assumed as elastic and isotropic, were employed as input in the simulations, as shown in Table I.

In this case, both tensile (Fig. 3C) and compressive (Fig. 3D) tests were performed along the two test directions, with the same boundary conditions specified previously. Compressive tests were run up to higher applied strains in order to account for progressive closure of pores during deformation. A contact check was therefore imposed on all pore surfaces (self-contact check in surface-to-surface mode, assuming a frictionless contact enforced using a penalty algorithm).

Elastic moduli were computed according to equation (1) as described above. In the compressive deformation case, the computation was performed at various ε_x and ε_y strain levels, in order to reconstruct the modulus vs. strain evolution, checking for stiffening phenomena due to pore closure.

3) Stationary heat transfer across HVOF-sprayed WC-CoCr was also simulated (using the OOF2 solver) by imposing a constant temperature of 673 K and 273 K at the top and bottom boundary, respectively. The normal heat flux \dot{Q} was integrated along the top boundary and the thermal conductivity κ was then obtained using Fourier's equation $\dot{Q} = \frac{\kappa}{L_y} \Delta T$, where ΔT = temperature gradient along the y direction (= 400 K in this case). Additional boundary conditions included zero normal heat flux at the right and left boundaries and plane temperature gradient (zero temperature gradient along the z direction).

The thermal properties of the various microstructural constituents are listed in Table 1.

4) Low magnification micrographs of hardmetal coatings were merged together into single, large-scale views of the coating (Fig. 4), covering a length equal to approximately 2.3 mm, as specified in Section 2.1. These micrographs were then turned into binary images representing a free-standing coating, with voids occupying the regions above and below it as well as the internal pore areas (Fig. 4).

Simulated static three-point bending tests were performed using both OOF2 and Abaqus finite element solvers. For greater simplicity, the hardmetal was assumed as isotropic, with elastic modulus equal to the E_y value modelled previously (see point 1) and $\nu = 0.30$. As the results in Section 4 will show, the anisotropy of the hardmetal coatings is not particularly marked, so that this approximation is not expected to lead to significant errors. Future work will consider the whole transversally isotropic stiffness matrix of the hardmetal coating to provide results that are even more accurate.

Zero displacement along the x and y directions was prescribed at the right support and zero y displacement was prescribed at the left support. A prescribed load P was applied on top of the beam, at the midpoint between the supports, and the resulting maximum displacement at the centre point of the beam (δ_{max}) was computed. Simulations were performed in plane stress condition, which is closer to the actual behaviour of a beam. The overall elastic modulus E of the material was extracted by the known relation (2) for simply supported beams:

$$\delta_{max} = \frac{Pl^3}{48EI} = \frac{P}{b} \frac{l^3}{4Eh^3} \quad (2)$$

Where:

l = distance between the supports;

$I = bh^3/12$ = moment of inertia of the beam section;

b, h = beam width and beam height.

The result was compared to the experimental value of the room-temperature storage modulus obtained by three-point bending tests (see Section 2.2). The size of the computational domain differs from that of the experimental sample described in Section 2.2 as the simulation of a 30 mm-long free-standing coating, viewed with sufficient resolution in order to capture porosity, would require very large images and, therefore, meshes with an extremely large number of elements. Nonetheless, the use of similar loading and constraining conditions ensures comparability between experimental and simulated results.

5) In order to reproduce the contact between a WC-CoCr hardmetal coating and a hard asperity on the surface of a counterbody in relative sliding motion, the geometry shown in Fig. 5A-C was implemented, where the hardmetal coating is in contact with a circular asperity of 1 μm radius, consisting of Al_2O_3 . A particularly fine mesh is generated close to the top surface of the WC-CoCr coating (Fig. 5D), in order to capture stress and strain gradients more precisely. Again, plane strain 6-node triangular elements and 8-node quadrangular elements were employed.

Whilst the alumina asperity, the WC phase and the oxide inclusions were simulated as purely elastic and isotropic, the matrix was in this case considered an elastic-plastic material (unlike the simulations previously described at point 1), in order to obtain a more realistic model, capable of reproducing micro-scale deformations and plastic flow behaviour. Material properties are listed in Table I. Due to the lack of specific data on the elastic-plastic properties of the CoCr-based matrix in HVOF-sprayed WC-CoCr hardmetals, the properties of a Co-Cr-W-C alloy (Stellite) were employed. This composition is probably close to that of the matrix phase of a HVOF-sprayed WC-CoCr hardmetal, since some dissolution of W and C in the Co-Cr phase inevitably occurs during HVOF spraying.

The loading procedure involved two stages. First, the asperity was pressed onto the coating surface, bounding it to move along the y direction only. The normal load was progressively increased up to 12.5 mN, in order to generate a nominal average contact pressure (computed according to the hertzian theory, assuming that the hardmetal coating is a purely elastic, isotropic, homogeneous material with elastic modulus $E = 400$ GPa) comparable to the coating hardness (≈ 14 GPa). In tribological pairings, it is indeed generally assumed (at least as a first approximation) that the pressure generated at the contact points between asperities is equal to the hardness of the softer of the mating surfaces [68]. Once the maximum normal load is reached, a displacement along the x direction is then imposed to the asperity in order to simulate relative sliding at constant velocity. Simulations were performed:

- either by assuming that the hardmetal coating is pinned along the bottom face, with displacements along the x -direction and rotations around the z -axis being forbidden along the left and right sides to account for the presence of surrounding material (Fig. 5B)
- or by assuming that the meshed microstructure is surrounded by an isotropic linear elastic material (Fig. 5C), the properties of which provide a simplified representation of the overall hardmetal ($E = 400$ GPa, $\nu = 0.30$).

Rotation of the asperity around the z direction is also prohibited, since, in real contact conditions, the asperity is attached to a larger body.

A frictional contact between the coating and the counterbody was enforced, assuming a friction coefficient $\mu = 0.5$. This constant value, chosen based on the experimental results detailed in [51], is a simplification, since the actual friction coefficient between the counterbody and the different phases of the coating (matrix, WC particles and oxide inclusions) may differ from point to point. In the absence of more detailed data on the friction coefficients of each material pairing, however, this simplification can lead to sufficiently accurate results, at least for a qualitative appreciation of the deformation mechanisms during sliding contact.

4. Results and discussion

4.1 *Micro-scale behaviour of HVOF-sprayed hardmetals*

In the case of HVOF-sprayed hardmetals (WC-CoCr, WC-FeCrAl), the predicted micro-scale elastic moduli along the x and y directions, computed according to the procedure described in Section 3, point 1), are in very good agreement with those obtained by depth-sensing micro-indentation (Section 2), as summarised in Fig. 6. In most cases, indeed, the difference between computed and experimentally measured values is smaller than the related standard deviation (plotted in Fig. 6 as error bar). The model is therefore capable of capturing the experimental (slight) anisotropy of these materials, the modulus on the plane of the lamellae (i.e. in the x -direction as defined in Fig. 2) being always somewhat higher than that in the transverse direction (y -direction, Fig. 2).

The results produced by different meshes (as shown in Fig. 2) do not differ significantly, provided the meshes are fine enough to satisfy the criterion of a homogeneity index ≥ 0.96 as laid out in Section 3, point 1. Similarly, different applied strains (as mentioned in Section 3, point 1) return identical elastic modulus values, which is obvious since all materials are assumed as purely elastic in these simulations, the purpose of which is to describe the elastic behaviour of the material only.

It should be noted that data on elastic modulus of the oxide inclusions, needed for the computations as explained in Section 3, can hardly be obtained experimentally, nor it is directly available from the literature. As many of the oxide inclusions appear to have been pulled out of the fracture surfaces of the hardmetal coatings (Fig. 7: the arrows indicate some of the voids left by the pull-out of oxide inclusions), they are inferred to contain a large amount of defects and to have poor cohesion and poor adhesion to the surrounding material. It is therefore reasonable to assume that the mechanical properties of the inclusions are comparable to those of a highly defective plasma-sprayed oxide, as listed in the literature; the corresponding value has therefore been employed, as listed in Table I.

In detail, the stress produced across the microstructure of hardmetal coatings by a tensile strain ε_x or ε_y is inhomogeneously distributed (Fig. 8): the stress obviously concentrates in the WC particles, by far the stiffest microstructural constituent (highest elastic modulus, Table I). “Veins” of stress are therefore seen in Fig. 8 where carbide particles are more numerous and contiguous, whereas regions with lower concentration of WC particles contribute less to the load-carrying behaviour.

Particularly severe stress concentrations arise in WC particles and in the nearby matrix in areas where oxide inclusions are more abundant and closer to one another. It may therefore be expected that, under actual applied loads, failure will first occur in these areas. This is confirmed by the propagation behaviour of the cracks found around some of the Berkovich micro-indentations performed as described in Section 2.2 (Fig. 9). Cracks, indeed, are generated when the indentation mark falls close to defective areas, propagating where more oxide inclusions are located (Fig. 9). This suggests that the effect of these inclusions surpasses the stress concentration generated at the indentation corners.

This behaviour can be modelled in two ways.

- (i) On the one hand, a microstructure with a fictitious triangular notch, having the same angles as a projected Berkovich indentation mark, can be subjected to the same uniform uniaxial tensile

strain $\varepsilon_y = 2\%$. Whilst this geometry cannot reproduce an indentation test, it can give a very useful indication on whether microstructural defects (oxide inclusions) can generate greater stress concentrations than a large-scale notch. The result of this model (Fig. 10), which is still run with purely elastic material properties as laid out in Section 3, point 1, clearly confirms that higher stress peaks are located next to the oxide inclusions, rather than at the tip of the large-scale triangular notch (see circled area in the σ_y stress distribution map of fig. 10), matching with the experimental observations from indentation testing (Fig. 9).

(ii) On the other hand, the extended finite element method (XFEM) implemented in the Abaqus software can be employed in order to simulate the initiation and propagation of a crack across the same notched microstructure shown in Fig. 10.

In this case, failure of the three microstructural constituents (WC, matrix and oxide) was assumed to begin at a prescribed maximum principal stress (Table I). A linear loss of strength after failure was assumed, until the energy stored by the material reaches the failure energy value listed in Table I. For a realistic representation of crack propagation behaviour, the matrix must now be modelled as an elastic-plastic material. As mentioned previously, obtaining full stress-strain curves for the matrix phase of thermal spray hardmetals is a particularly difficult task. The FeCrAl matrix of this hardmetal was therefore modelled as a bilinear material, i.e. the plastic portion of the stress-strain curve of the material was assumed linear between the yield strength and ultimate tensile strength values obtained from the literature for FeCrAl-type alloys (Table I). In order to avoid unrealistically high levels of stresses and plastic strains, the applied strain in this simulation was reduced to $\varepsilon_y = 0.3\%$ (Fig. 11).

The results (Fig. 11) confirm that, whilst a short crack develops at the tip of the notch, the main crack propagates slightly away from the notch, inside a WC particle located between two oxide inclusions (see arrows), where a particularly severe stress concentration occurs.

Microstructure-based finite element models can therefore be extended even beyond the quantitative prediction of the elastic modulus of the material, and can return (at least qualitative) information on

the role of microstructural features for crack initiation. However, in this case, the simulation clearly becomes very sensitive to the selection of a wide range of material properties (including elastic-plastic behaviours, failure loads and fracture energies, etc.), which may not be easily available.

Heat conduction across hardmetal coatings is also not homogeneous at the microstructural level (Fig. 12). Similar to the stress distribution seen in Fig. 8, indeed, preferential paths for heat flow exist where WC particles are more numerous and contiguous, since the thermal conductivity of WC (Table I) is much higher than that of the matrix and of the oxide inclusions (again assumed to be comparable to a defective, thermally sprayed oxide).

The overall thermal conductivity in the 20 – 400 °C range, computed from the model results as described in Section 3, point 3), is $\kappa_{model} = (33.5 \pm 2.5) \text{ W/(m}\cdot\text{K)}$, which matches remarkably well with the literature value $\kappa_{exp} = 29 \text{ W/(m}\cdot\text{K)}$ [44]. This provides further validation to the reliability of these micro-scale thermal and mechanical models.

4.2 Micro-scale behaviour of APS Cr_2O_3

Under tensile deformation, the computed elastic modulus of APS Cr_2O_3 is $E_y = 59.5 \pm 22.7 \text{ GPa}$ along the y-direction and $E_x = 91.5 \pm 28.4 \text{ GPa}$ along the x-direction (directions are defined as in Fig. 3 and 13A). The former value compares well with the experimental result $E_{y,exp} = 46.6 \pm 4.0 \text{ GPa}$ obtained by depth-sensing Berkovich micro-indentation (Section 2.2). The significant standard deviations associated to the model results are due to the local microstructural variability of the material, so that a quite large number of micrographs are needed in order to have representative values. Nonetheless, even with as low as 6 micrographs, average values which approach the experimental results are obtained. Future studies and practical implementations of the technique should certainly aim to include a higher amount of micrographs.

When a compressive stress is applied, the internal faces of pores and defects (most of which are elongated along the interlamellar direction, Fig. 3) come into contact (see Fig. 13B-D). As the applied strain grows larger, pores continue closing and stress transfer across their contacting faces increases (Fig. 13D), so that the reconstructed stress-strain behaviour of the material is non-linear (Fig. 14A).

Consistently with the previously discussed scatter in the local microstructural characteristics of the material, different micrographs (the results of four of them are plotted in Fig. 14 for better clarity) return slightly different trends. Correspondingly, the local elastic modulus has some variability (Fig. 14B), but, in all cases, a progressive stiffening is obvious.

These trends match quite well with the experimental graphs obtained for similar plasma-sprayed ceramic coatings under compressive loading in [46,47,58,69], corroborating to the validity of these FE models.

4.3 *Macro-scale behaviour of HVOF-sprayed hardmetals*

As clearly seen in Fig. 4, HVOF-sprayed hardmetal possess much lower porosity than APS Cr_2O_3 . In the latter case, therefore, experimental or numerical analyses at the micro-scale already reflect the mechanical influence of such porosity. Pores and defects in APS Cr_2O_3 , indeed, significantly affect the depth-sensing indentation response at an applied load of 3 N; similarly, the high-magnification SEM micrographs (such as those in Figs. 3 and 13) are already accounting for the presence of such porosity. On the other hand, as pores in HVOF-sprayed hardmetals are fewer and more scattered, numerical analyses on micrographs which are magnified enough to tell the various microstructural constituents (such as those in Figs. 1, 2, 8) do not account for such pores. Similarly, micro-indentation tests at 3 N load are quite insensitive to them. Indentations are indeed generally not performed on locations where pores are present and, should an indentation happen to fall on or very close to a pore, its load-penetration curve would differ so much from all others to result in it being discarded from the overall data set.

Larger-scale mechanical tests are therefore needed in order to capture the macroscopic mechanical behaviour of hardmetal coatings, accounting for the characteristic size-dependency discussed e.g. in [42,43]. The three point bending test on free-standing coating (Section 2.2) and the corresponding model (Fig. 15) were therefore implemented.

The value obtained by three-point bending as described in Section 2.2 ($E' = 150$ GPa) and that extracted from the model results based on equation (2) as described in Section 3 ($E = 158$ GPa) are in excellent agreement. Both succeed in capturing the expected scaling behaviour of mechanical properties, the macro-scale modulus being lower than the micro-scale one (Section 4.1 and Fig. 6) because of the effect of the pore seen in Fig. 3.

4.4 *Asperity contact modelling*

As recalled in Section 3, point 5, the tribological contact between mating surfaces, particularly when they both possess high hardness, is concentrated on very small (micrometre-sized) asperities [50]. A conventional macro-scale model can only simulate the contact of ideally smooth shapes, but the local stress distribution at micro-scale asperity contacts can be significantly different, so that, once again, a microstructure-based model is needed. Accordingly, the issue of micro-scale contacts in composite materials and coatings very recently started to be addressed in the literature [40,70]. The result of the model presented in Fig. 5 specifically highlights some very interesting and significant features.

First, the distribution of contact stresses between a micrometre-sized, purely elastic Al_2O_3 asperity and the hardmetal coating is far from what would be predicted by the hertzian model in a homogeneous material (Fig. 16A,B). To the contrary, the stress concentrates in the carbide particles, hence irradiating along “veins” where these particles are more numerous and contiguous, a result which resembles that obtained in [40,70] and which is also perfectly consistent with the previous observations based on simpler uniaxial tensile models in Section 4.1. This is clearly due to the much greater stiffness of the WC phase compared to the matrix, which, apart from a lower elastic

modulus (Table I), is also modelled as a bi-linear elastic-plastic material: its stiffness therefore degrades further as extensive yielding occurs near the contact region, increasing the stress concentration in the WC phase. These stress “veins” can clearly have significant effects on the local behaviour of the material. Stresses of the order of some GPa in the WC particles can certainly lead to their failure and fragmentation, a known wear phenomenon in hardmetals [71].

As the asperity, once pressed inside the material, is dragged forward, the stress peak increases, exceeding 2 GPa both in the WC particles and in the asperity itself (Fig. 16D,F). The pattern of the stress “veins” changes and moves ahead of the indenter (Fig. 16D,F), and the material in the vicinity of the surface is plastically deformed (Fig. 16C,E). Specifically, the matrix, whose stiffness is extensively degraded by yielding, is extruded into rough “waves”, a detail of which can be seen in Fig. 16G, and drags the finest WC particles as well.

This behaviour is perfectly well matched by the actual observation of worn WC-CoCr hardmetal samples after dry ball-on-disk sliding against an Al_2O_3 counterpart. Fig. 16H accordingly shows an SEM micrograph of one such surface, as previously obtained in [51]. The surface has indeed been deformed into a rough, “wavy” morphology, where the WC particles are displaced at an angle with the pristine surface plane as a consequence of sliding. The same behaviour has been repeatedly observed by the authors for WC-based hardmetal coatings subjected to sliding contact against hard counterparts at room temperature [51,72,73]. On the actual surface (as seen in Fig. 16H as well as in all the mentioned references), the matrix cannot be seen any more, as its extrusion ends up in its eventual removal.

The actual removal of the matrix is hardly grasped by FE models as these would require a lot of data on the deformation and failure behaviour of the matrix phase under large plastic strains and high strain rates (which is normally unavailable). The present results are, however, of the utmost relevance as they shed a new light on the micro-scale deformation behaviour underlying the onset of the wear mechanisms, which are experimentally observed at the end of a tribological test.

5. Conclusions

This paper showed a series of examples demonstrating how microstructure-based finite element modelling procedures can be applied to the interpretation and prediction of the thermo-mechanical behaviour of thermal spray coatings, with particular reference to HVOF-sprayed hardmetals (WC-CoCr, WC-FeCrAl) and to APS Cr_2O_3 . Comparison to experimental and/or literature data allowed for validation of the models.

It was shown that simple microstructure-based models performed with purely elastic material behaviour can return reliable values for the elastic moduli at the micro-scale, in good agreement with those obtained by depth-sensing indentation testing. The model results reflect the intrinsic anisotropy (transverse isotropy) of thermal spray coatings and, particularly for highly porous plasma-sprayed ceramic oxides, it can reproduce the stiffening behaviour under compressive loading.

The model can therefore provide more information than experiments do. For instance, in the case of porous APS ceramics, measurements of in-plane elastic modulus by indentation testing on a polished top surface are hardly possible, due to the likely generation of pull-out artefacts during grinding, which can alter the measured properties. Measuring the progressive stiffening during crack closure also requires complex, time-consuming experimental procedures, which are often unaffordable particularly in an industrial R&D context.

The model can similarly predict the through-thickness thermal conductivity of hardmetals, with good match to literature values.

Microstructural models performed at different length scales can also reproduce the scaling behaviour of the mechanical properties of thermal spray coatings (from the micro- to the macro-scale), reflecting e.g. the difference between the micro-scale elastic modulus by depth-sensing indentation and the macro-scale modulus by three-point bending tests.

Modelling of more complex material behaviours requires an accurate knowledge of the plastic and failure properties (experimental plastic strain vs. stress data, maximum stress/strain at failure, fracture energy, etc.), which may be difficult to obtain for the individual constituents of a thermal spray coating, particularly because of the occurrence of structural and chemical alterations during the deposition process.

Nonetheless, reasonable estimates of those properties allow the prediction of crack initiation locations, particularly highlighting the relevance of stress concentrations around some peculiar microstructural defects such as oxide inclusions in a hardmetal coating, which can be even more dangerous than a macroscopic notch.

Similarly, the micro-scale deformation behaviour during sliding contact with small-scale hard asperities highlights the fundamental mechanisms underlying the overall tribological behaviour observed after wear testing. It was indeed possible to reproduce the local plastic flow and extrusion of the matrix out of the hardmetal surface during sliding contact with a small asperity of an alumina counterbody, which accounts for the roughened, “wavy” morphology observed on actual wear surfaces after ball-on-disk testing.

Acknowledgements

The authors are grateful to Prof. Massimo Messori (University of Modena and Reggio Emilia) for performing the three-point bending tests.

Many thanks to Mr. Tim Börner for the installation of the OOF2 software.

References

- [1] National Research Council (U.S.) Committee on Coatings for High-Temperature Structural Materials, Coatings for High-Temperature Structural Materials: Trends and Opportunities, National Academy Press, Washington D.C., USA, 1996.
- [2] The European Technology Platform for Advanced Engineering Materials and Technologies – EuMaT, Strategic Research Agenda – 2nd Edition, Steinbeis-Edition, Stuttgart, Germany, 2012. Available on-line at: <http://eumat.eu/filehandler.ashx?file=11580> (last accessed 24/05/2013).
- [3] ISO 6892-1:2009. Metallic materials - Tensile testing - Part 1: Method of test at room temperature. International Organization for Standardization (ISO), Geneva, Switzerland, 2009.
- [4] J.R. Davis (Ed.), Handbook of Thermal Spray Technology, ASM International, Materials Park, OH, USA, 2004, pp. 171-213.
- [5] M. Vilémová, J. Matějčíček, R. Mušálek, J. Nohava, Application of Structure-Based Models of Mechanical and Thermal Properties on Plasma Sprayed Coatings, J. Therm. Spray Technol. 21 (3-4) (2012) 372–382.
- [6] M. Li, P.D. Christofides, Modeling and Control of High-Velocity Oxygen-Fuel (HVOF) Thermal Spray: A Tutorial Review, J. Therm. Spray Technol. 18(5-6) (2009) 753-768.
- [7] B. Klusemann, R. Denzer, B. Svendsen, Microstructure-Based Modeling of Residual Stresses in WC-12Co-Sprayed Coatings, J. Therm. Spray Technol. 21(1) (2012) 96–107.
- [8] L. Wang, Y. Wang, X.G. Sun, Z.Y. Pan, J.Q. He, C.G. Li, Influence of pores on the surface microcompression mechanical response of thermal barrier coatings fabricated by atmospheric plasma spray—Finite element simulation, Appl. Surf. Sci. 257(6) (2011) 2238–2249.
- [9] N. Chawla, B.V. Patel, M. Koopman, K.K. Chawla, R. Saha, B.R. Patterson, E.R. Fuller, S.A. Langer, Microstructure-based simulation of thermomechanical behavior of composite materials by object-oriented finite element analysis, Mater. Charact. 49(5) (2002) 395–407.
- [10] S. Katani, F. Madadi, M. Atapour, S. Ziaei Rad, Micromechanical modelling of damage behaviour of Ti–6Al–4V, Mater. Des. 49 (2013) 1016–1021.
- [11] S. Sodjit, V. Uthaisangasuk, Microstructure based prediction of strain hardening behavior of dual phase steels, Mater. Des. 41 (2012) 370–379.
- [12] H. Hosseini-Toudeshky, B. Anbarlooie, J. Kadkhodapour, Micromechanics stress–strain behavior prediction of dual phase steel considering plasticity and grain boundaries debonding, Mater. Des. 68 (2015) 167–176.
- [13] Y. Liu, L. Cheng, Q. Zeng, Z. Feng, J. Zhang, J. Peng, C. Xie, K. Guan, Monte Carlo simulation of polycrystalline microstructures and finite element stress analysis, Mater. Des. 55 (2014) 740–746.

- [14] T. Sirinakorn, S. Wongwiset, V. Uthaisangskul, A study of local deformation and damage of dual phase steel, *Mater. Des.* 64 (2014) 729–742.
- [15] Y. Jiang, K. Qiu, Computational micromechanics analysis of toughening mechanisms of particle-reinforced bulk metallic glass composites, *Mater. Des.* 65 (2015) 410–416.
- [16] G.G. Sozhamannan, S. Balasivanandha Prabu, R. Paskaramoorthy, Failures analysis of particle reinforced metal matrix composites by microstructure based models, *Mater. Des.* 31 (2010) 3785–3790.
- [17] M. Yu, P. Zhu, Yingqi Ma, Effects of particle clustering on the tensile properties and failure mechanisms of hollow spheres filled syntactic foams: A numerical investigation by microstructure based modeling, *Mater. Des.* 47 (2013) 80–89.
- [18] H. Qing, Automatic generation of 2D micromechanical finite element model of silicon–carbide/aluminum metal matrix composites: Effects of the boundary conditions, *Mater. Des.* 44 (2013) 446–453.
- [19] H. Qing, 2D micromechanical analysis of SiC/Al metal matrix composites under tensile, shear and combined tensile/shear loads, *Mater. Des.* 51 (2013) 438–447.
- [20] S. Wei, W. Fu-chi, F. Qun-bo, M. Zhuang, Lifetime prediction of plasma-sprayed thermal barrier coating systems, *Surf. Coat. Technol.* 217 (2013) 39–45.
- [21] M. Ranjbar-Far, J. Absi, G. Mariaux, Finite Element Modeling of the Different Failure Mechanisms of a Plasma Sprayed Thermal Barrier Coatings System, *J. Therm. Spray Technol.* 21(6) (2012) 1234–1244.
- [22] M. Ranjbar-Far, J. Absi, G. Mariaux, F. Dubois, Simulation of the effect of material properties and interface roughness on the stress distribution in thermal barrier coatings using finite element method, *Mater. Des.* 31 (2010) 772–781.
- [23] M. Ranjbar-Far, J. Absi, G. Mariaux, D.S. Smith, Crack propagation modeling on the interfaces of thermal barrier coating system with different thickness of the oxide layer and different interface morphologies, *Mater. Des.* 32 (2011) 4961–4969.
- [24] J.-H. Qiao, R. Bolot, H. Liao, P. Bertrand, C. Coddet, A 3D finite-difference model for the effective thermal conductivity of thermal barrier coatings produced by plasma spraying, *Int. J. Therm. Sci.* 65 (2013) 120–126.
- [25] L. Wang, Y. Wang, X.G. Sun, J.Q. He, Z.Y. Pan, C.H. Wang, A novel structure design towards extremely low thermal conductivity for thermal barrier coatings – Experimental and mathematical study, *Mater. Des.* 35 (2012) 505–517.
- [26] T. Wiederkehr, B. Klusemann, D. Gies, H. Müller, B. Svendsen, An image morphing method for 3D reconstruction and FE-analysis of pore networks in thermal spray coatings, *Comput. Mater. Sci.* 47 (2010) 881–889.

- [27] S. Wei, W. Fu-chi, F. Qun-Bo, M. Zhuang, Effects of defects on the effective thermal conductivity of thermal barrier coatings, *Appl. Math. Modell.* 36 (2012) 1995–2002.
- [28] Z. Wang, A. Kulkarni, S. Deshpande, T. Nakamura, H. Herman, Effects of pores and interfaces on effective properties of plasma sprayed zirconia coatings, *Acta Mater.* 51 (2003) 5319–5334.
- [29] N. Ramanujam, T. Nakamura, Erosion mechanisms of thermally sprayed coatings with multiple phases, *Surf. Coat. Technol.* 204 (2009) 42–53.
- [30] J.-H. Qiao, R. Bolot, H. Liao, Finite element modeling of the elastic modulus of thermal barrier coatings, *Surf. Coat. Technol.* 220 (2013) 170–173.
- [31] A. Zivelonghi, F. Cernuschi, C. Peyrega, D. Jeulin, S. Lindig, J.H. You, Influence of the dual-scale random morphology on the heat conduction of plasma-sprayed tungsten via image-based FEM, *Comput. Mater. Sci.* 68 (2013) 5–17.
- [32] Y. Wang, J. Hua, Z. Liu, Y. Zeng, Y. Zhou, H. Wang, Melting index characterization and thermal conductivity model of plasma sprayed YSZ coatings, *J. Eur. Ceram. Soc.* 32 (2012) 3701–3707.
- [33] A. Zivelonghi, A. Brendel, S. Lindig, S. Nawka, B. Kieback, J.H. You, Microstructure-based analysis of thermal- and mechanical behaviors of W/CuCrZr composites and porous W coating, *J. Nucl. Mater.* 417 (2011) 536–539.
- [34] H.I. Faraoun, J.L. Seichepine, C. Coddet, H. Aourag, J. Zwick, N. Hopkins, D. Sporer, M. Hertter, Modelling route for abradable coatings, *Surf. Coat. Technol.* 200 (2006) 6578–6582.
- [35] R. Bolot, J.-L. Seichepine, J.H. Qiao, C. Coddet, Predicting the Thermal Conductivity of AlSi/Polyester Abradable Coatings: Effects of the Numerical Method, *J. Therm. Spray Technol.* 20(1-2) (2011) 39–47.
- [36] S. Wei, W. Fu-chi, F. Qun-bo, H. Dan, M. Zhuang, Proposal of new expressions for effects of splat interfaces and defects on effective properties of thermal barrier coatings, *Surf. Coat. Technol.* 204 (2010) 3376–3381.
- [37] C.-H. Hsueh, E.R. Fuller Jr., Residual stresses in thermal barrier coatings: effects of interface asperity curvature: height and oxide thickness, *Mater. Sci. Eng. A* 283 (2000) 46–55.
- [38] F. Azarmi, T. Coyle, J. Mostaghimi, Young's modulus measurement and study of the relationship between mechanical properties and microstructure of air plasma sprayed alloy 625, *Surf. Coat. Technol.* 203 (2009) 1045–1054.
- [39] P. Michlik, C. Berndt, Image-based extended finite element modeling of thermal barrier coatings, *Surf. Coat. Technol.* 201 (2006) 2369–2380.
- [40] K. Holmberg, A. Laukkanen, A. Ghabchi, M. Rombouts, E. Turunen, R. Waudby, T. Suhonen, K. Valtonen, E. Sarlin, Computational modelling based wear resistance analysis of thick composite coatings, *Tribol. Int.* 72 (2014) 13–30.

- [41] OOF project website: <http://www.ctcms.nist.gov/oof/oof2/> (last accessed 24/05/2013).
- [42] J. Nohava, B. Bonferroni, G. Bolelli, L. Lusvarghi, Interesting aspects of indentation and scratch methods for characterization of thermally-sprayed coatings, *Surf. Coat. Technol.* 205(4) (2010) 1127–1131.
- [43] N. Margadant, J. Neuenschwander, S. Stauss, H. Kaps, A. Kulkarni, J. Matejcek, G. Rössler, Impact of probing volume from different mechanical measurement methods on elastic properties of thermally sprayed Ni-based coatings on a mesoscopic scale, *Surf. Coat. Technol.* 200 (8) (2006) 2805–2820.
- [44] S. Thiele, K. Sempf, K. Jaenicke-Roessler, L.-M. Berger, J. Spatzier, Thermophysical and Microstructural Studies on Thermally Sprayed Tungsten Carbide-Cobalt Coatings, *J. Therm. Spray Technol.* 20(1-2) (2011) 358-365.
- [45] N. Spinicchia, G. Angella, R. Benocci, A. Bruschi, A. Cremona, G. Gittini, A. Nardone, E. Signorelli, E. Vassallo, Study of plasma sprayed ceramic coatings for high power density microwave loads, *Surf. Coat. Technol.* 200 (2005) 115 –1154.
- [46] R. Musalek, J. Matejcek, M. Vilemova, O. Kovarik, Non-Linear Mechanical Behavior of Plasma Sprayed Alumina Under Mechanical and Thermal Loading, *J. Therm. Spray Technol.* 19(1-2) (2010) 422–428.
- [47] F. Kroupa, Nonlinear Behavior in Compression and Tension of Thermally Sprayed Ceramic Coatings, *J. Therm. Spray Technol.* 16(1) (2007) 84–95.
- [48] O. Kovářík, J. Siegl, J. Nohava, P. Chráska, Young's Modulus and Fatigue Behavior of Plasma-Sprayed Alumina Coatings, *J. Therm. Spray Technol.* 14(2) (2005) 231-238
- [49] F. Kroupa, J. Dubsky, Pressure dependence of Young's moduli of thermal sprayed materials, *Scripta Mater.* 40(11) (1999) 1249-1254.
- [50] M.F. Ashby, J. Abulawi, H.S. Kong, Temperature Maps for Frictional Heating in Dry Sliding, *Tribol. Trans.* 34(4) (1991) 577-587.
- [51] G. Bolelli, I. Hulka, H. Koivuluoto, L. Lusvarghi, A. Milanti, K. Niemi, P. Vuoristo, Properties of WC-FeCrAl coatings manufactured by different high velocity thermal spray processes, *Surf. Coat. Technol.* 247 (2014) 74–89.
- [52] H. Warlimont, *Ceramics*, in: W. Martiensden, H. Warlimont (eds.), *Springer Handbook of Condensed Matter and Materials Data*, Springer, Berlin, Germany, 2005, pp. 462-463.
- [53] www.matweb.com (last accessed 17/07/2014).
- [54] S.G. Huang, K. Vanmeensel, O. Van der Biest, J. Vleugels, Binderless WC and WC–VC materials obtained by pulsed electric current sintering, *Int. J. Refract. Met. Hard Mater.* 26 (2008) 41–47.

- [55] Stellite-6 product data sheet:
http://stellite.com/Portals/0/KMT_Stellite_6Alloy_Data_FINAL.pdf (last accessed 17/07/2014)
- [56] Product datasheet for Kanthal A-1 Fe-Cr-Al alloy: <http://kanthal.com/en/products/material-datasheets/strip/kanthal-a-1/> (last accessed 17/07/2014)
- [57] O. Kovářík, J. Siegl, J. Nohava, P. Chráska, Young's Modulus and Fatigue Behavior of Plasma-Sprayed Alumina Coatings, *J. Therm. Spray Technol.* 14(2) (2005) 231-238.
- [58] R.W. Trice, C. Batson, C. Sharff, K.T. Faber, The role of starting powder size on the compressive response of stand-alone plasma-sprayed alumina coatings, *J. Mater. Sci.* 37 (2002) 629-636.
- [59] Y.-Z. Xing, Q.-L. Wei, J.-M. Hao, The fracture toughness of alumina coatings plasma-sprayed at different in situ temperatures, *Ceram. Int.* 38 (2012) 4661-4667.
- [60] Y. Wang, H. Fang, C.L. Zacherl, Z. Mei, S. Shang, L.-Q. Chen, P.D. Jablonski, Z.-K. Liu, First-principles lattice dynamics, thermodynamics, and elasticity of Cr_2O_3 , *Surf. Sci.* 606 (2012) 1422-1425.
- [61] R.S. Lima, S.E. Kruger, G. Lamouche, B.R. Marple, Elastic Modulus Measurements via Laser-Ultrasonic and Knoop Indentation Techniques in Thermally Sprayed Coatings, *J. Therm. Spray Technol.* 14(1) (2005) 52-60.
- [62] R.S. Lima, B.R. Marple, Near-isotropic air plasma sprayed titania, *Acta Mater.* 52 (2004) 1163-1170.
- [63] S.-H. Leigh, C.-K. Lin, C.C. Berndt, Elastic Response of Thermal Spray Deposits under Indentation Tests, *J. Am. Ceram. Soc.*, 80(8) (1997) 2093-2099.
- [64] S.-H. Leigh, C.C. Berndt, Modelling of elastic constants of plasma spray deposits with ellipsoid-shaped voids, *Acta Mater.* 47(5) (1999) 1575-1586.
- [65] W.C. Oliver, G.M. Pharr, Improved technique for determining hardness and elastic modulus using load and displacement sensing indentation experiments, *J. Mater. Res.* 7(6) (1992) 1564-1580.
- [66] ISO 14577-1:2002. Metallic materials - Instrumented indentation test for hardness and materials parameters - Part 1: Test method. International Organization for Standardization (ISO), Technical Committee 164/Subcommittee 3, Geneva, Switzerland, 2002.
- [67] ISO 14577-4:2007. Metallic materials -- Instrumented indentation test for hardness and materials parameters -- Part 4: Test method for metallic and non-metallic coatings. International Organization for Standardization (ISO), Geneva, Switzerland, 2007.
- [68] K. Kato, K. Adachi, Wear Mechanisms, in: B. Bhushan (Ed.), *Modern Tribology Handbook – Volume One*, CRC Press, Boca Raton, FL, USA, 2001, p. 279.

- [69] R.W. Trice, D.W. Prine, K.T. Faber, Deformation Mechanisms in Compression-Loaded, Stand-Alone Plasma-Sprayed Alumina Coatings, *J. Am. Ceram. Soc.* 83(12) (2000) 3057–3064.
- [70] K. Holmberg, A. Laukkanen, E. Turunen, T. Laitinen, Wear resistance optimisation of composite coatings by computational microstructural modelling, *Surf. Coat. Technol.* 247 (2014) 1–13.
- [71] M.G. Gee, A. Gant, B. Roebuck, Wear mechanisms in abrasion and erosion of WC/Co and related hardmetals, *Wear* 263 (2007) 137–148.
- [72] G. Bolelli, L.-M. Berger, M. Bonetti, L. Lusvarghi, Comparative study of the dry sliding wear behaviour of HVOF-sprayed WC–(W,Cr)₂C–Ni and WC–CoCr hardmetal coatings, *Wear* 309(1–2) (2014) 96–111.
- [73] G. Bolelli, T. Börner, F. Bozza, V. Cannillo, G. Cirillo, L. Lusvarghi, Cermet coatings with Fe-based matrix as alternative to WC–CoCr: Mechanical and tribological behaviours, *Surf. Coat. Technol.* 206(19–20) (2012) 4079–4094.

Figure captions

Figure 1. (A) Cross-sectional SEM micrograph (backscattered electrons) of a WC – 15wt.%FeCrAl coating deposited using a gas-fuelled Diamond Jet 2700 HVOF torch and (B) the same micrograph after image processing for phase identification (white = FeCrAl matrix; grey = WC; black = oxide inclusions).

Figure 2. Different kinds of FE meshes created on the processed micrograph of Fig. 1B: (A) quadrangular elements only (detail in inset) or (B) mixed quadrangular + triangular elements.

Panel A also shows the schematics of the boundary conditions employed for simulated uniaxial tensile testing along the y direction.

Figure 3. (A) Cross-sectional SEM micrograph (backscattered electrons) of an APS Cr₂O₃. (B) the same micrograph after image processing for phase identification (white = Cr₂O₃; black = pores), and FE meshes built on the processed micrograph, with boundary conditions for simulated uniaxial tensile (C) and compressive (D) tests along the y direction.

Figure 4. Example of the generation of a simulated free-standing coating image by merging of low-magnification SEM micrographs (backscattered electrons) of a Diamond Jet 2700-HVOF sprayed WC-FeCrAl hardmetal.

Figure 5. (A) Cross-sectional SEM micrograph (backscattered electrons) of a HVOF-sprayed WC-CoCr coating, (B) FE meshing of the micrograph and of a circular counterbody, with detail of the refinement in the contact area, (C) contact model with boundary conditions applied on the microstructure, and (D) contact model with the meshed microstructure surrounded by homogeneous material.

Figure 6. Elastic modulus of various hardmetal coatings along the x and y directions (as defined in Fig. 2): comparison between experimental values (by depth-sensing micro-indentation) and FE modelling predictions.

Figure 7. Fracture surfaces of HVOF-sprayed WC-FeCrAl coatings deposited by the DiamondJet 2700 (A) and JP5000 (B) processes. The arrows indicate pulled-out oxide inclusions.

Figure 8. Cross-sectional SEM micrograph of a HVOF-sprayed WC-FeCrAl hardmetal coating and corresponding distribution of the computed (OOF2 software) σ_y stress as a consequence of a $\varepsilon_y = 2\%$ applied strain.

Figure 9. Cracks propagating from the corner of a Berkovich indentation mark in a JP5000-HVOF sprayed WC-FeCrAl hardmetal coating.

Figure 10. Simulation of a uniaxial tensile test (OOF2 software) on a JP5000-HVOF sprayed WC-FeCrAl coating with a fictitious triangular notch.

Figure 11. Simulation of crack propagation (ABAQUS software) during uniaxial tensile strain of a JP5000-HVOF sprayed WC-FeCrAl coating with a fictitious triangular notch.

Figure 12. Image processing of a SEM micrograph of a HVOF-sprayed WC-CoCr hardmetal coating and result of microstructure-based stationary heat flow modelling.

Figure 13. Von Mises stress distribution during compressive deformation of the APS Cr_2O_3 microstructure shown in Fig. 3D: (A) overview at the maximum applied strain $\epsilon_y = -2.5\%$, and details at no applied strain (B), at initial crack closure (C) and at maximum applied strain (D).

Figure 14. Modelled stress-strain curves of APS Cr_2O_3 during uniaxial compression (A) and resulting trend of elastic modulus vs. applied strain (B).

Figure 15. FE model of a three-point bending test on the reconstructed free-standing DJ2700-HVOF sprayed WC-FeCrAl hardmetal coating shown in Fig. 4.

Figure 16. Results of micro-scale modelling of a single-asperity contact according to the model outlined in Fig 5D.

Overview (A) and detail (B) of the Von Mises stress distribution at the end of the asperity loading stage; deformed configurations (C,E) and Von Mises stress distributions (D,F) at various stages of sliding; greater detail of the deformed configuration of panel E (G) and SEM micrograph (H) of the

surface of a HVOF-sprayed WC-CoCr hardmetal after actual ball-on-disk sliding against sintered Al_2O_3 (details in [51]).

ACCEPTED MANUSCRIPT

Tables

Table I. Material properties employed in FE simulations.

Legend: $\sigma_{p,fail}$ = maximum principal stress at the beginning of failure;
 σ_y = yield strength;
 σ_{plast} , ε_{plast} = stress and corresponding plastic strain at a representative point
 G_{IC} = failure energy (stored energy corresponding to complete material degradation)
 κ = thermal conductivity;
 c_p = specific heat

Material	WC [52]	CoCr(W) [55]	FeCrAl [56]	Oxide inclusions	Hardmetal (homogeneous)	Cr ₂ O ₃ [60]	Al ₂ O ₃ [53]
E [GPa]	700	207	220	10 [57]	400	309	370
ν	0.24	0.30	0.30	0.15	0.30	0.28	0.23
σ_y [MPa]	/	895	460	/	/	/	/
σ_{plast} [MPa]	/	925	670	/	/	/	/
ε_{plast}	/	0.048	0.22	/	/	/	/
$\sigma_{p,fail}$ [MPa]	280 ¹⁾	/	470	120 ³⁾	/	/	/
G_{IC} [J/m ²]	25 ²⁾	/	260	100 ⁴⁾	/	/	/
κ [W/(m·K)]	121	14 [53]	/	2 [45]	/	/	/

¹⁾ approximately 1/10 of the compressive strength according to [53]

²⁾ computed from the plane-strain relation $G_{IC} = K_{IC}^2 * (1 - \nu^2) / E$ with $K_{IC} \approx 4 \text{ MPa} \cdot \text{m}^{1/2}$ [54]

³⁾ assumed to be around 1/5 of the compressive strength according to [58]

⁴⁾ computed from the plane-strain relation $G_{IC} = K_{IC}^2 * (1 - \nu^2) / E$ with $K_{IC} \approx 1 \text{ MPa} \cdot \text{m}^{1/2}$ [59].

Highlights

Microstructure-based finite element models simulate the properties of thermal spray coatings

Modelled values of orthotropic elastic moduli agree with experimental measurements

Compressive stiffening of plasma sprayed ceramics occurs by progressive crack closure

Cracks initiate where defects (e.g. oxide inclusions) cause stress concentration

Single-asperity contact models reveal microscale stress propagation and plastic flow

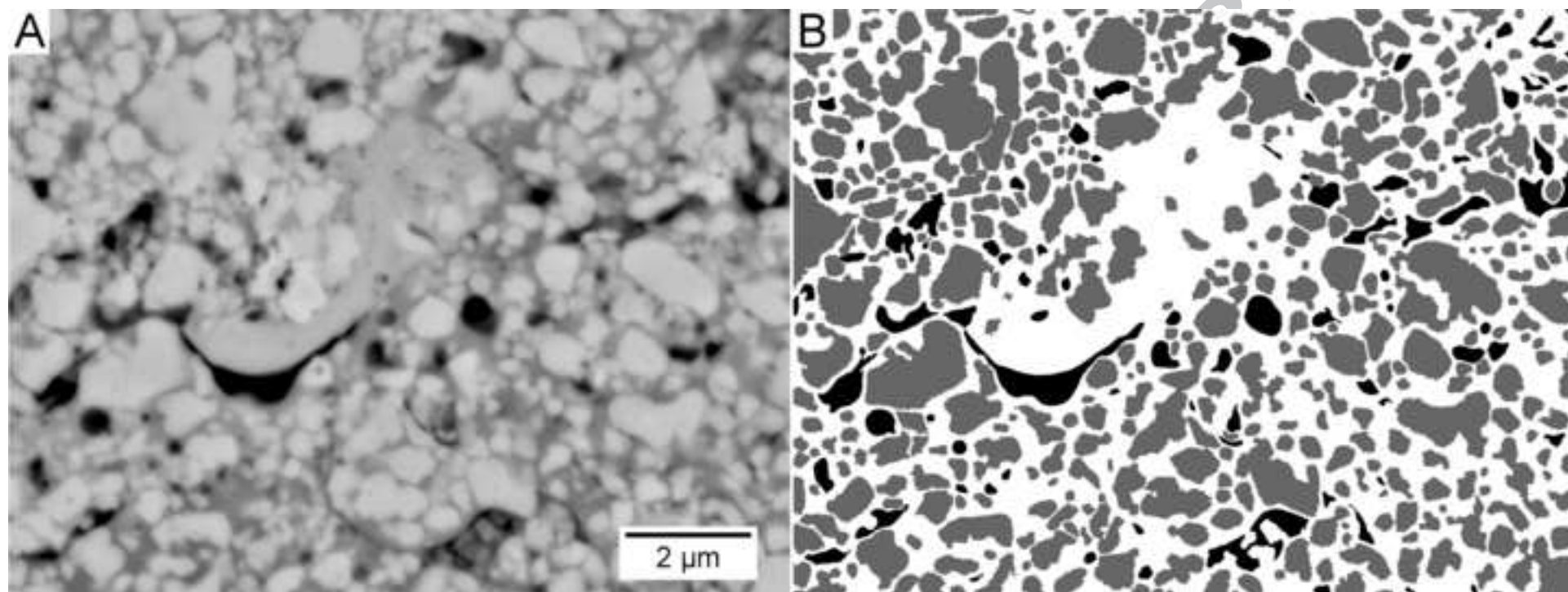


Figure 2

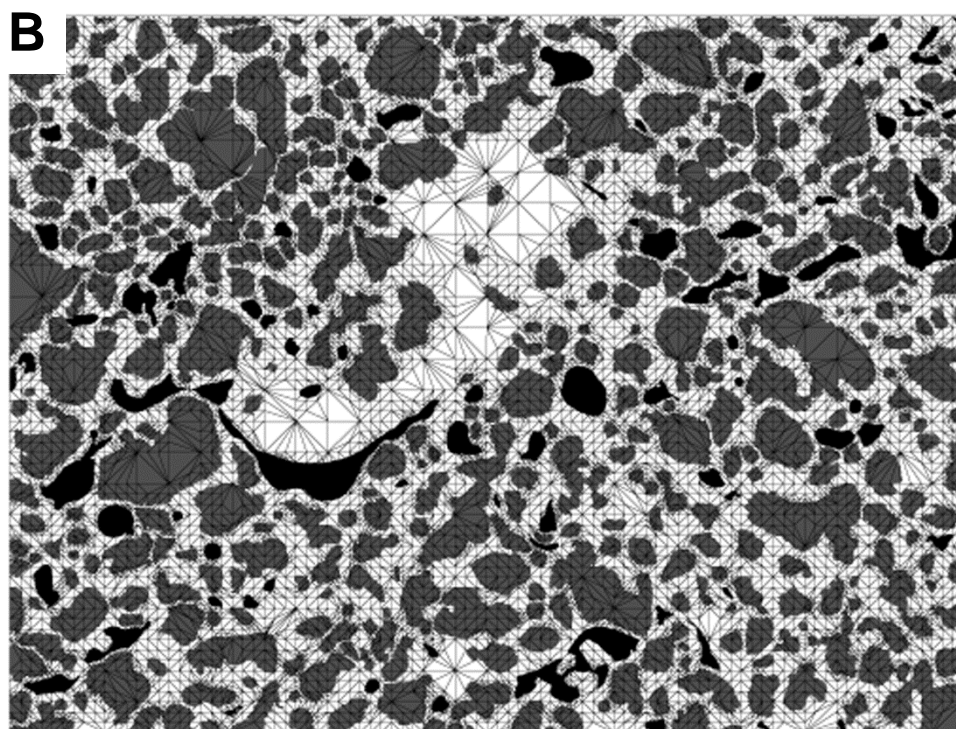
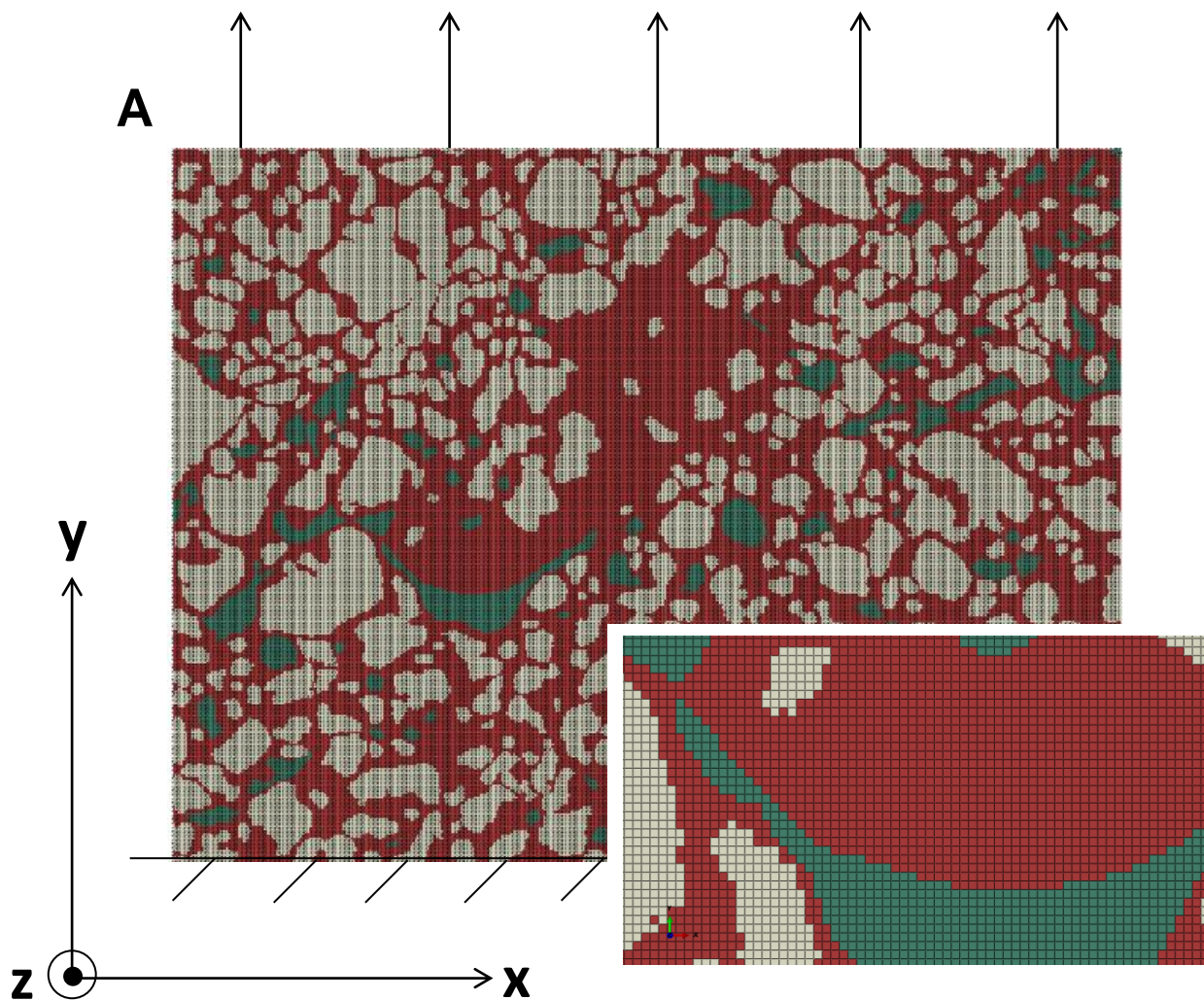


Figure 3

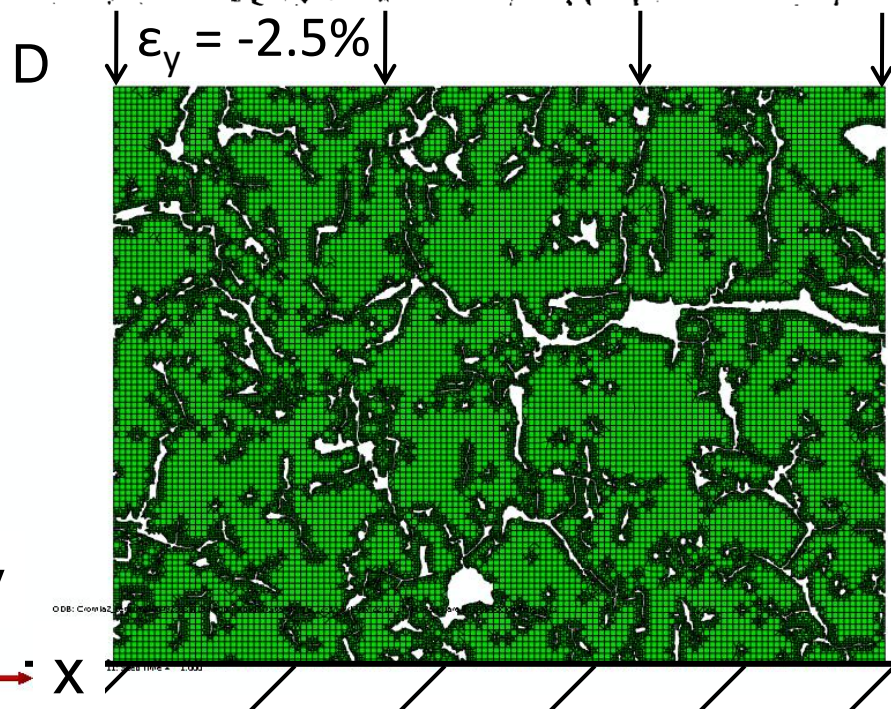
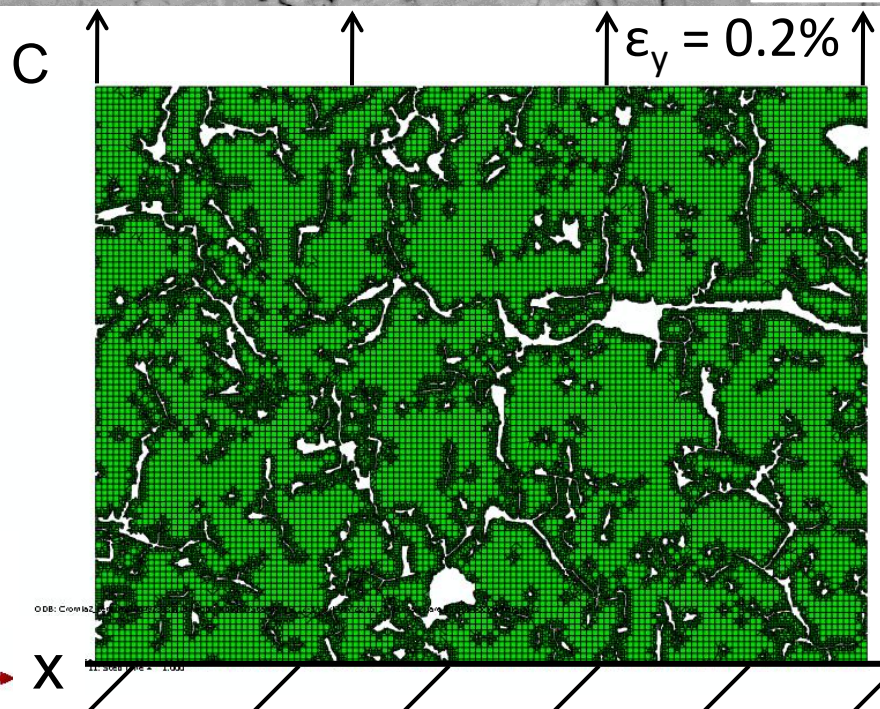
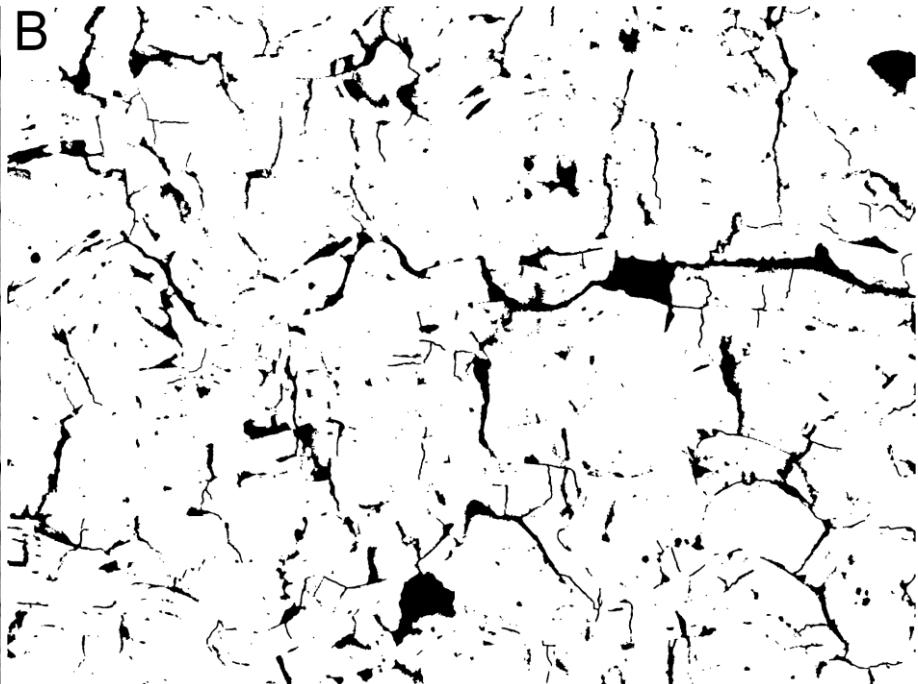
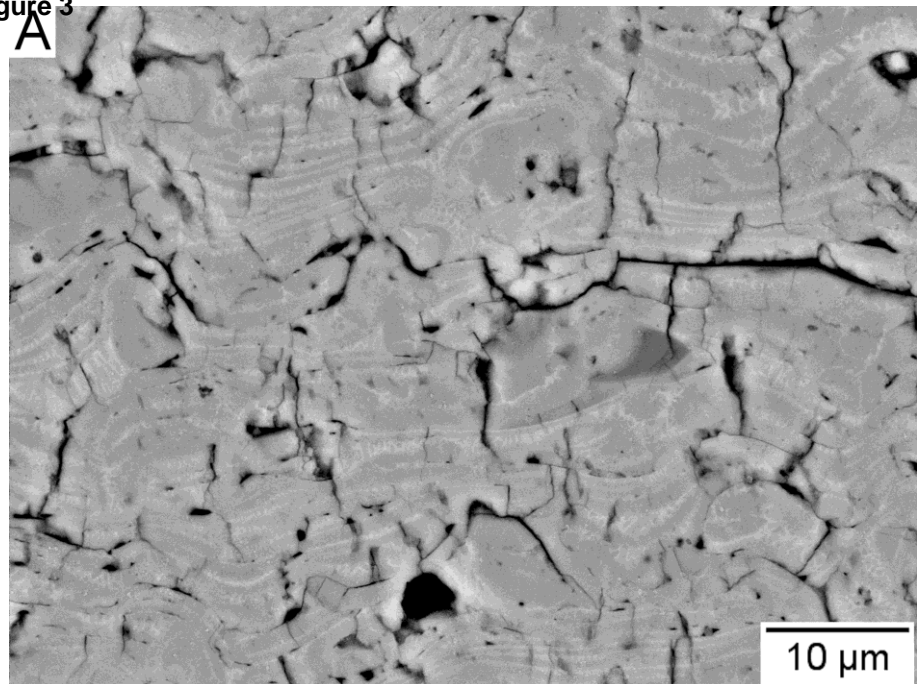
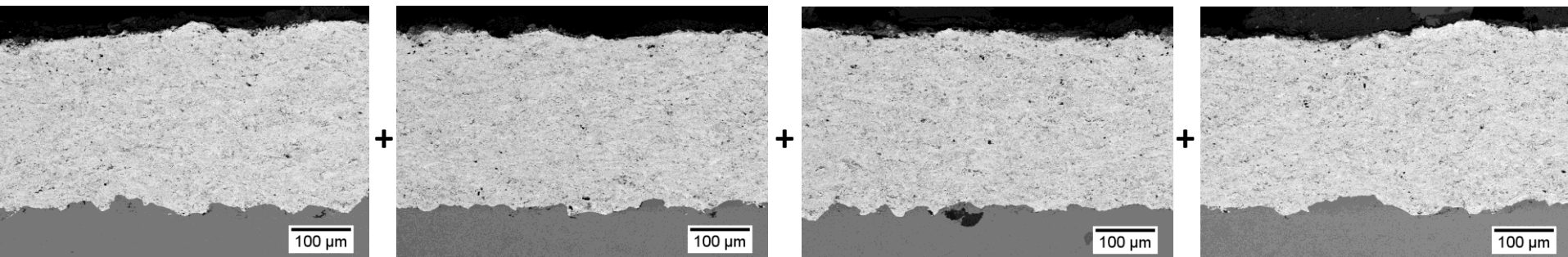
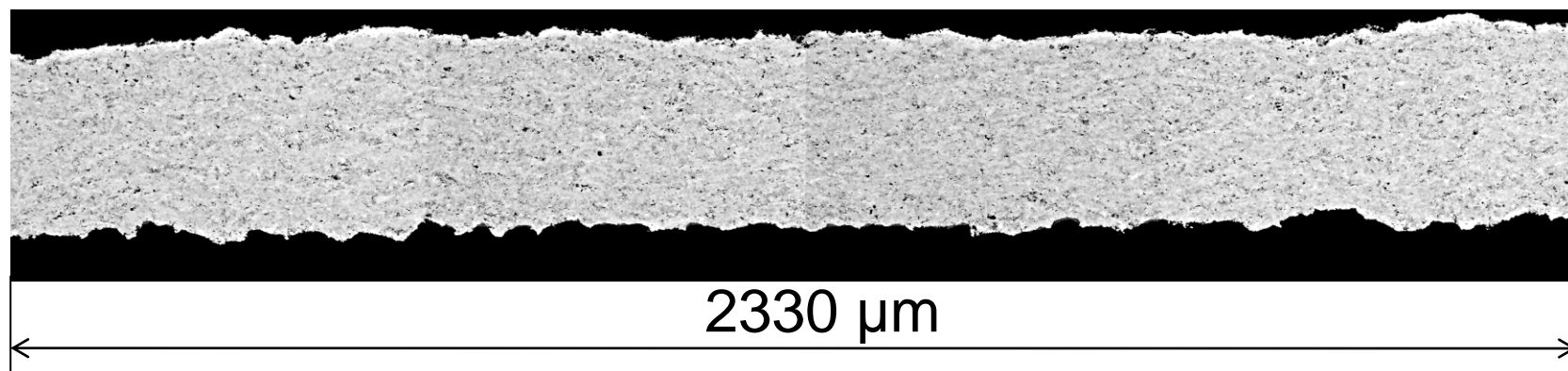


Figure 4

SEM MICROGRAPHS



MERGED MICROGRAPHS



SIMULATED FREE-STANDING COATING

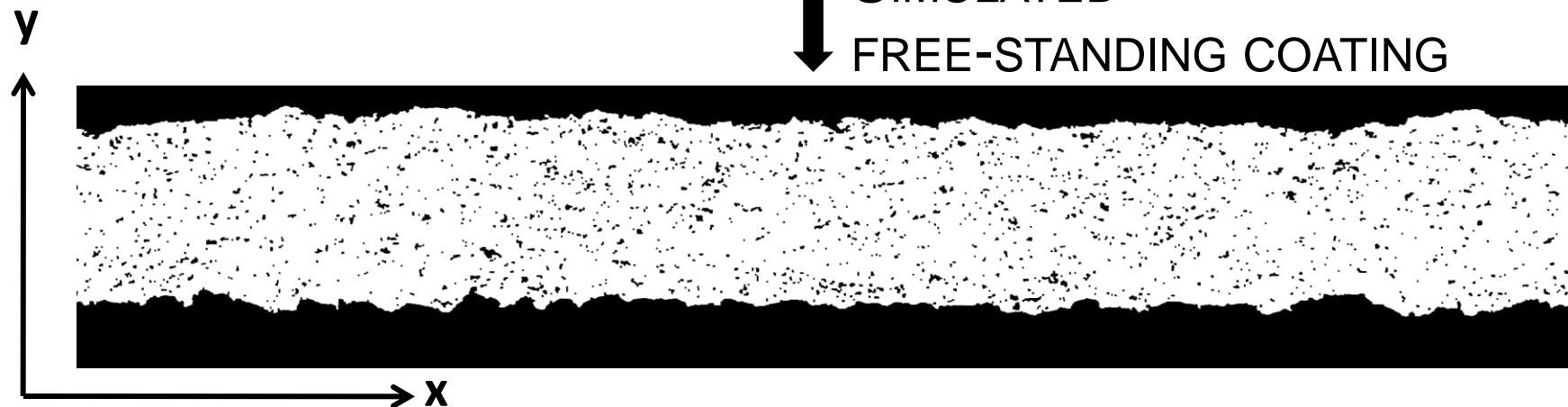
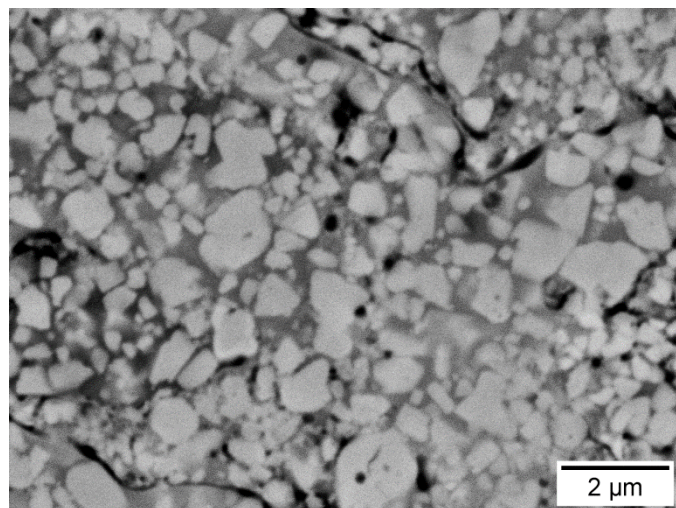
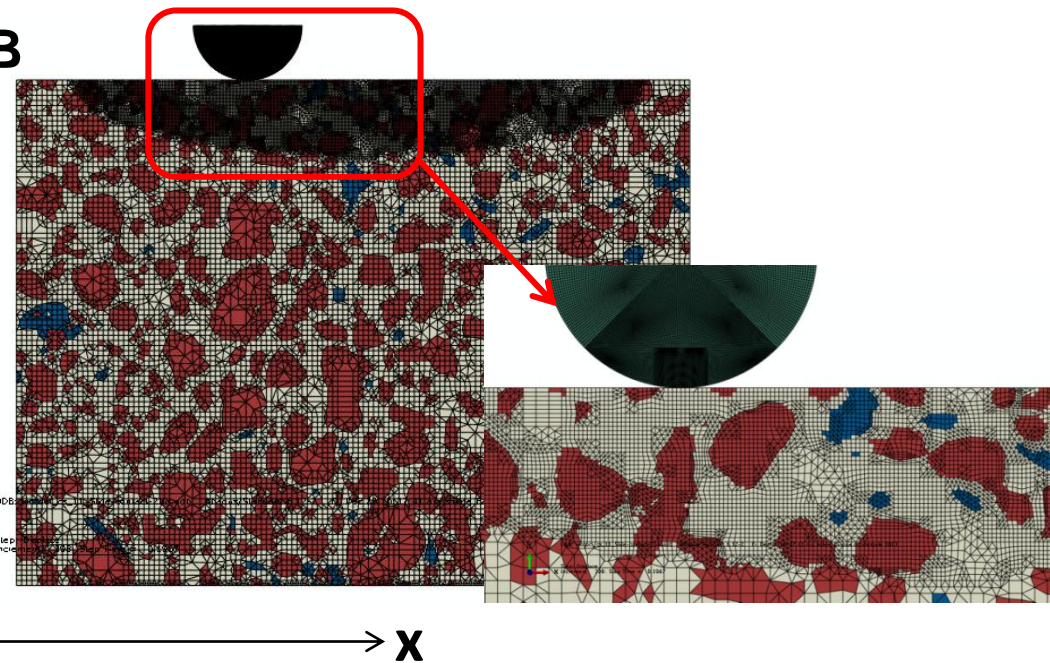


Figure 5

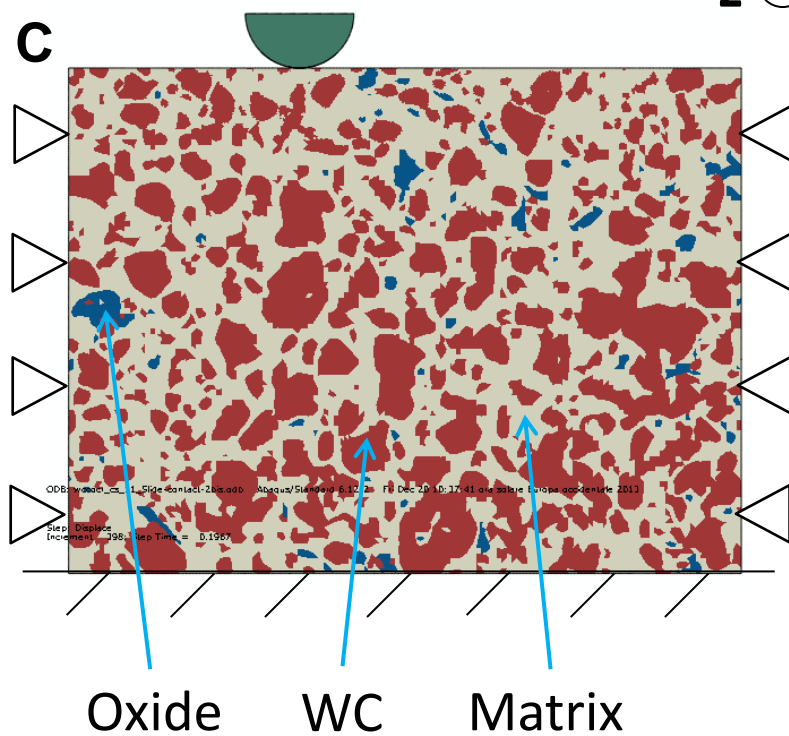
A



B



C



D

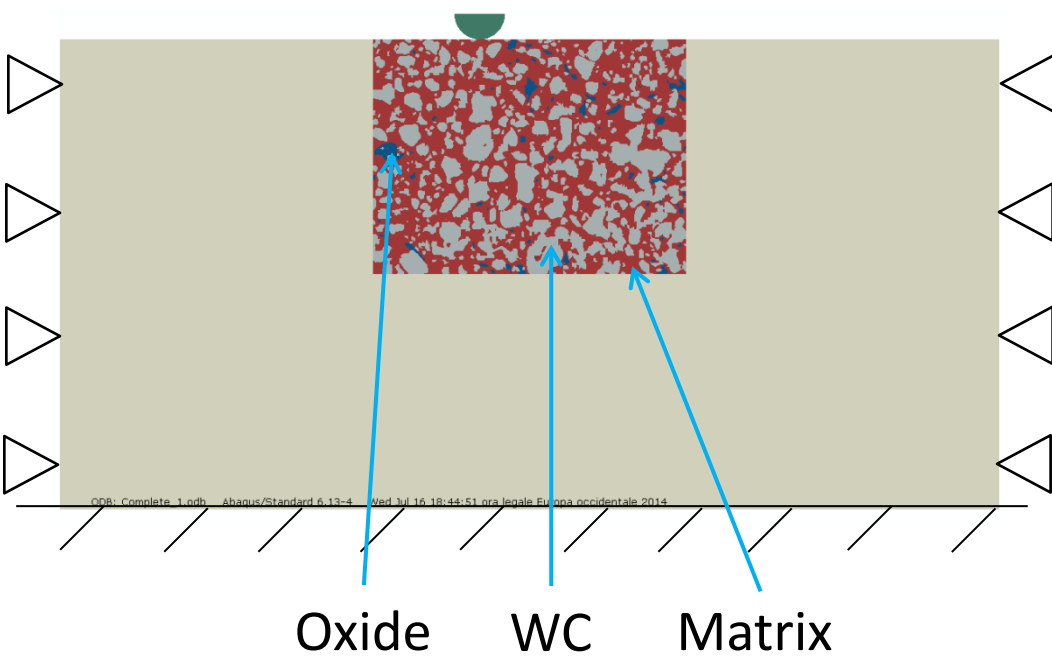


Figure 6

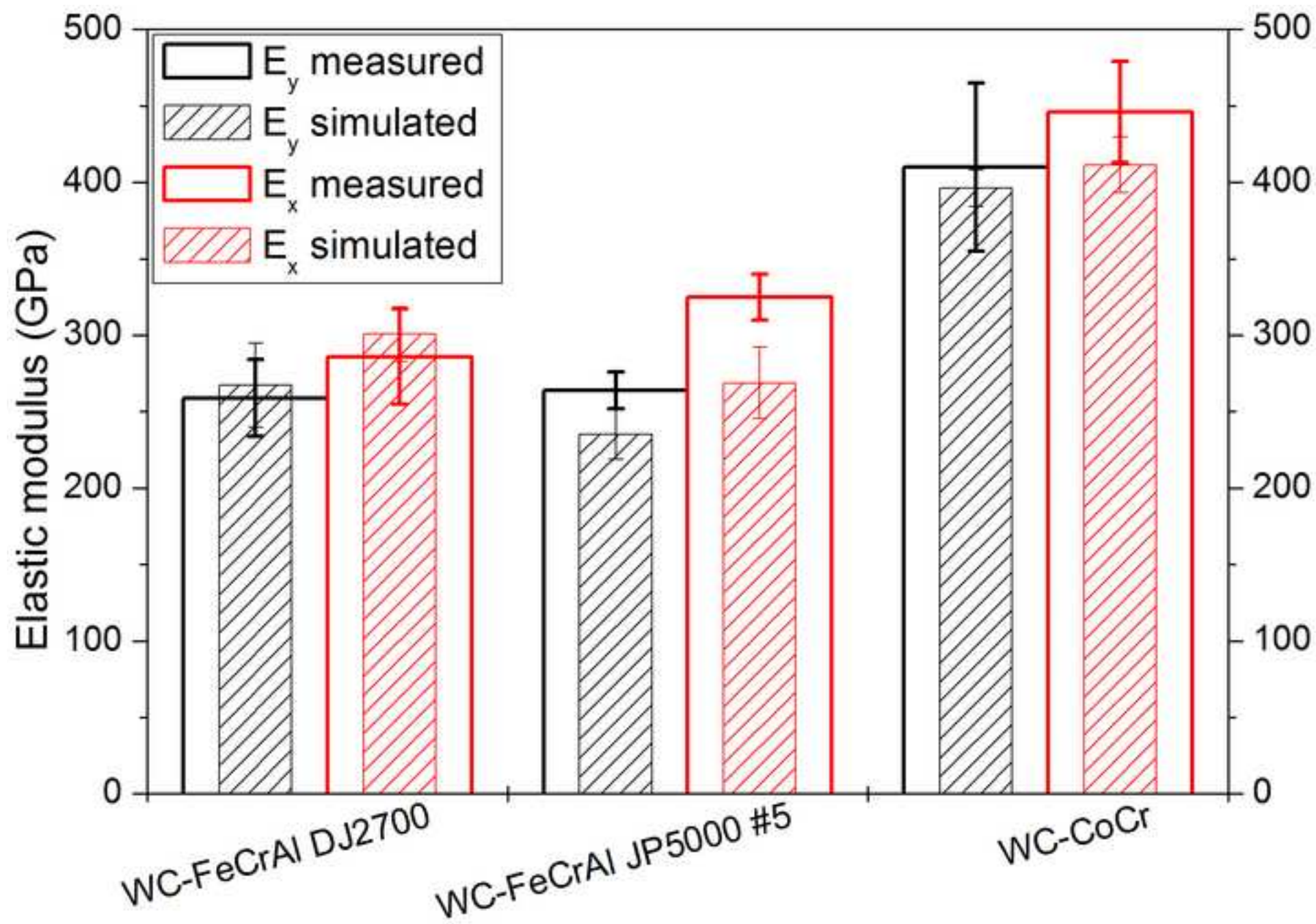


Figure 7

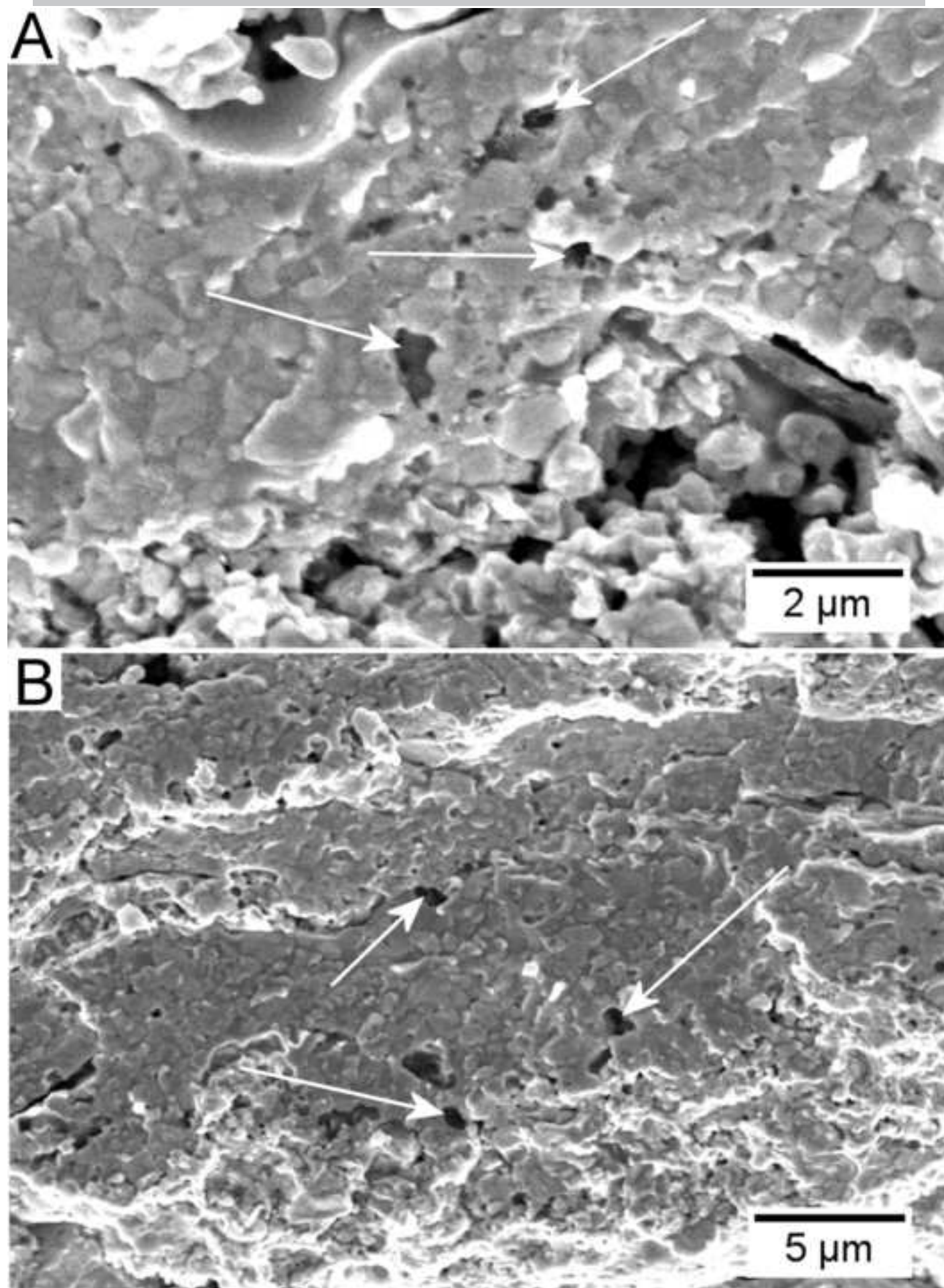


Figure 8

$$\varepsilon_y = 2 \text{ ‰}$$

σ_y STRESS DISTRIBUTION

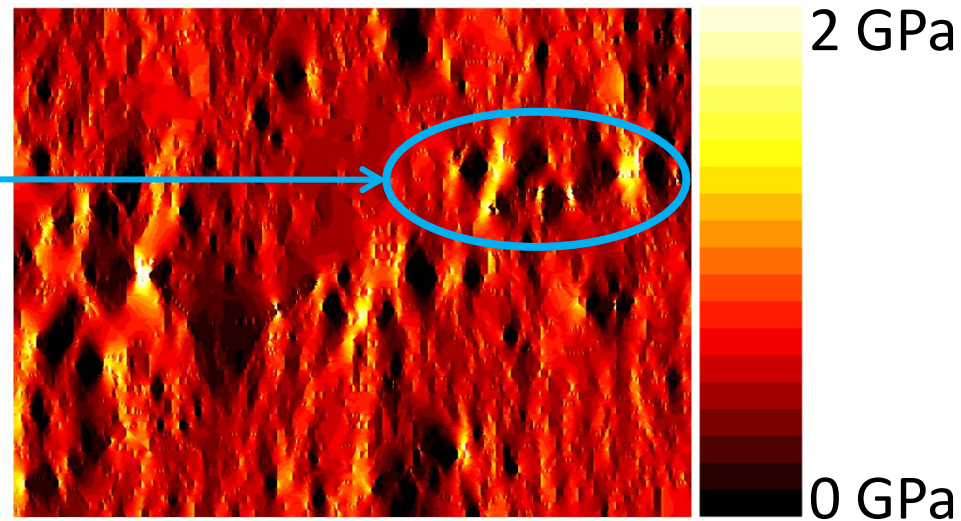
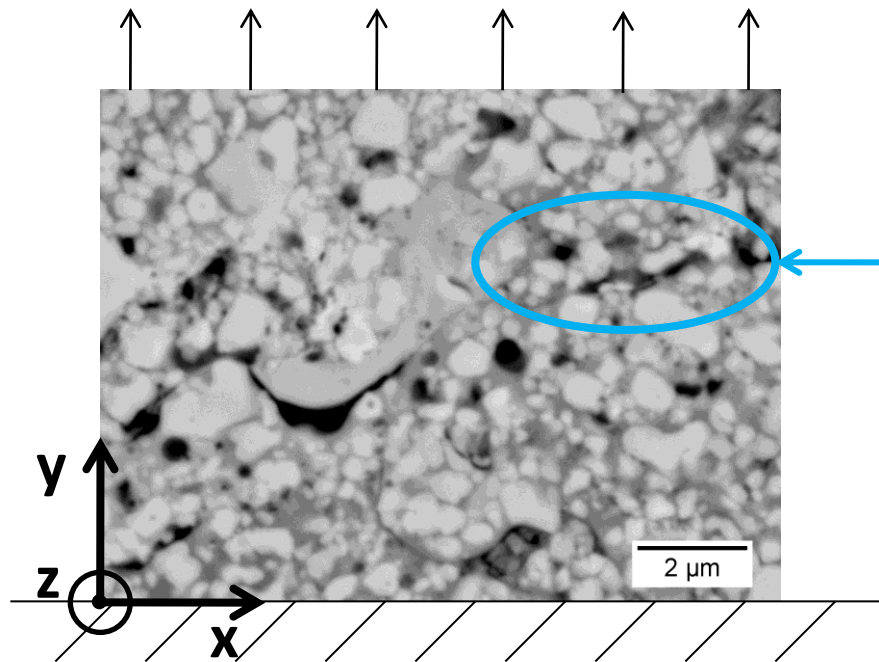


Figure 9

ACCEPTED MANUSCRIPT

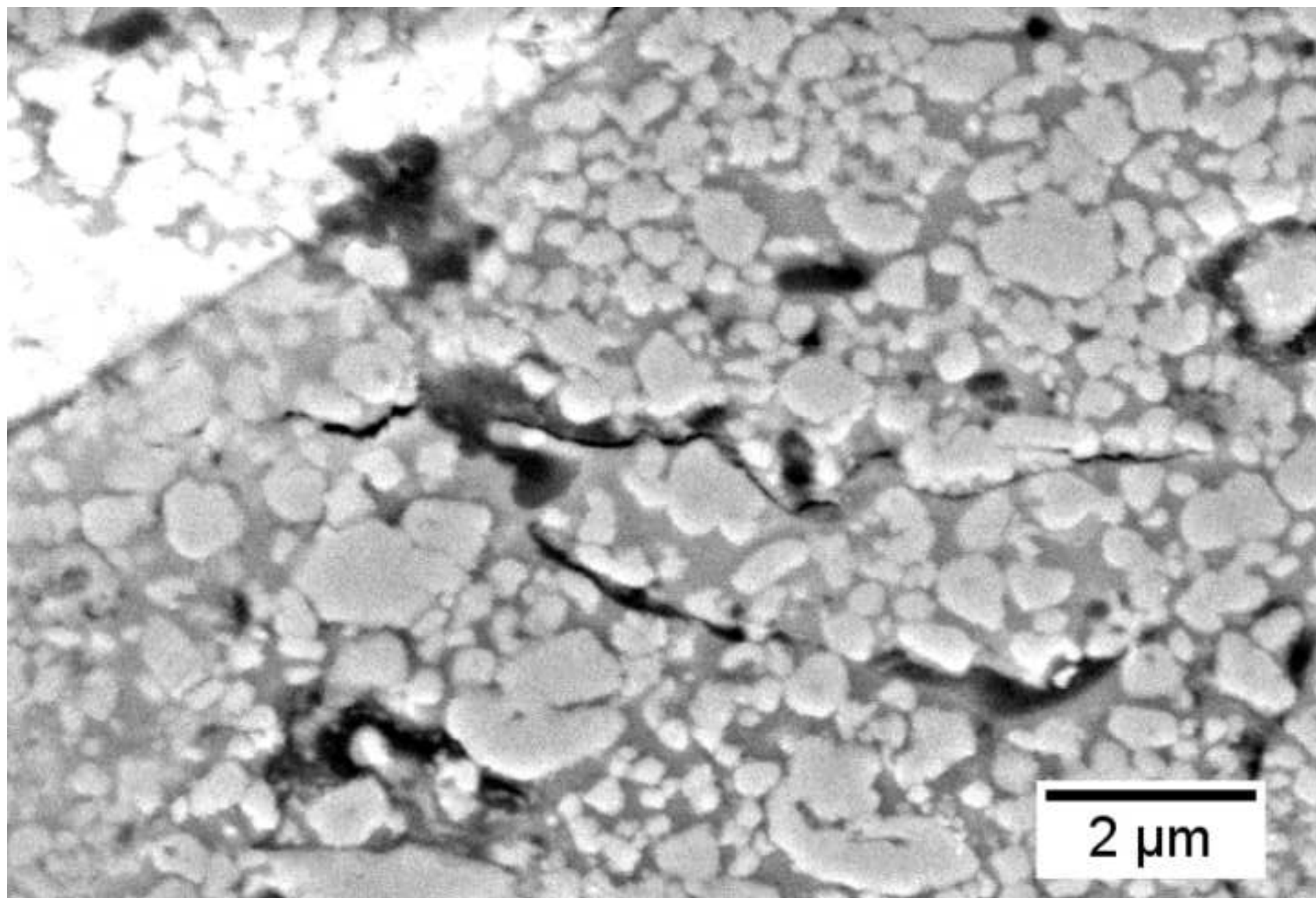
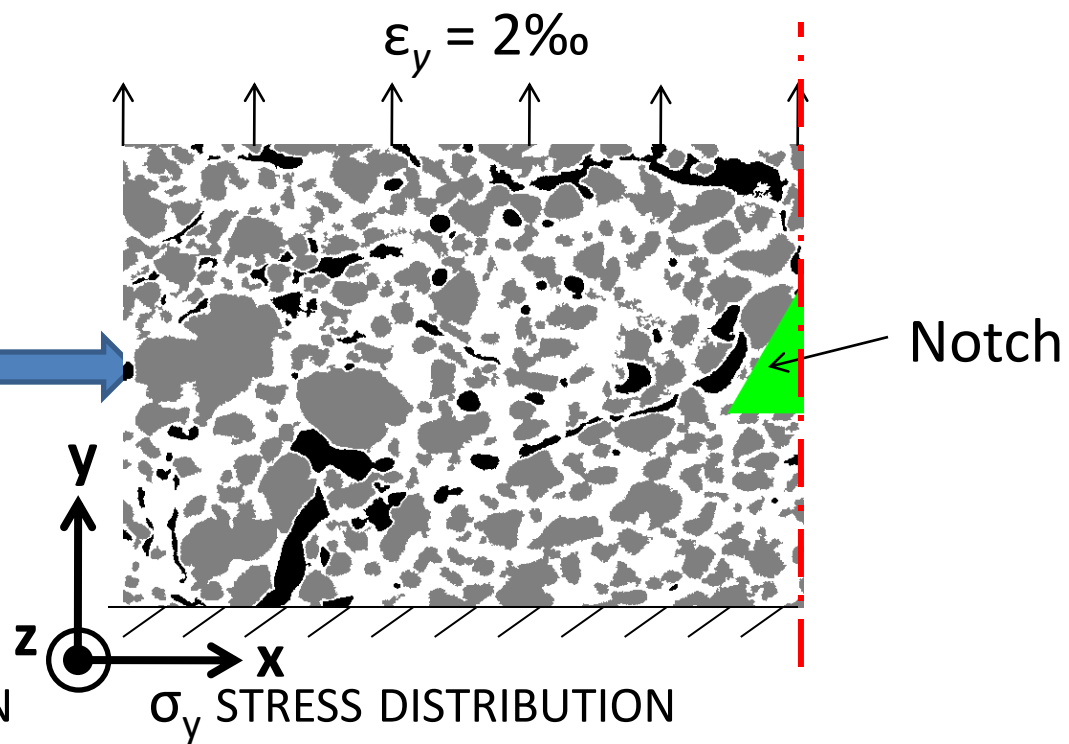
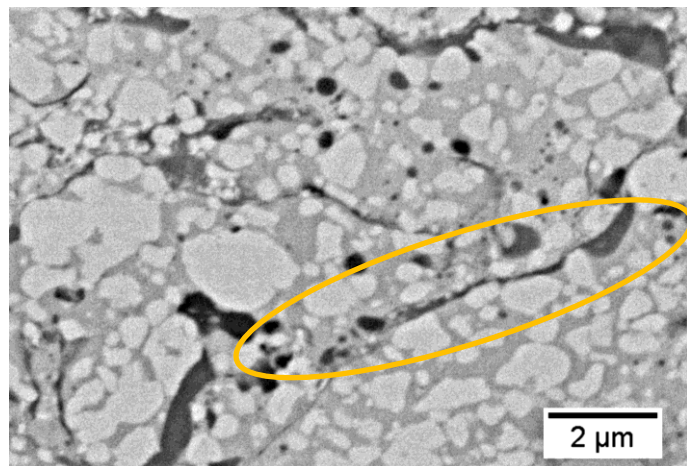


Figure 10

SEM MICROGRAPH



MESH + IMAGE RECONSTRUCTION

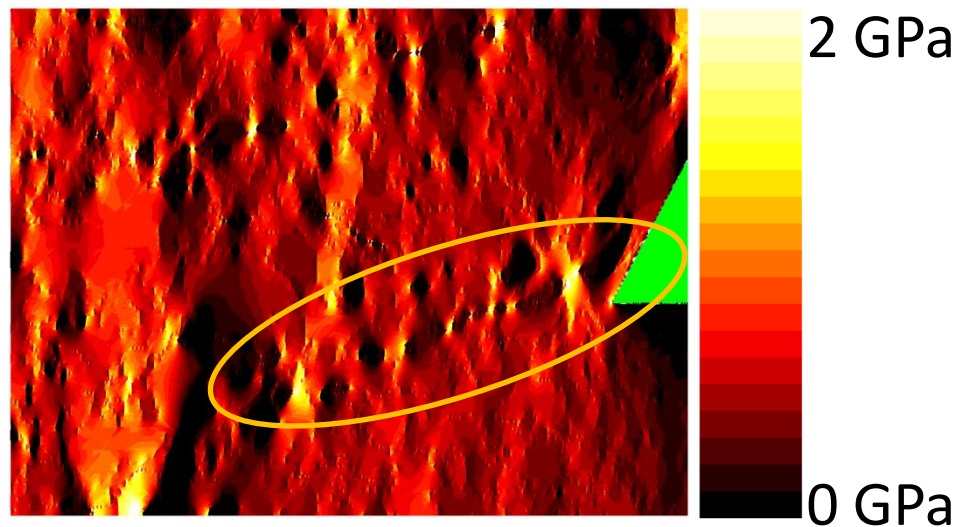
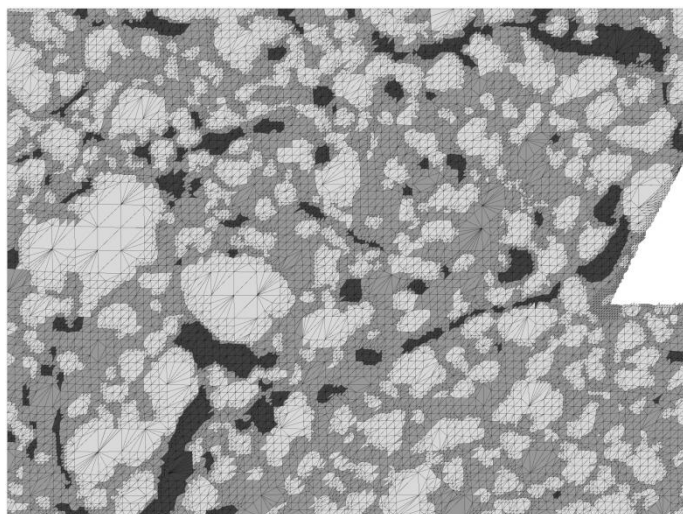
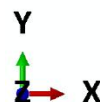
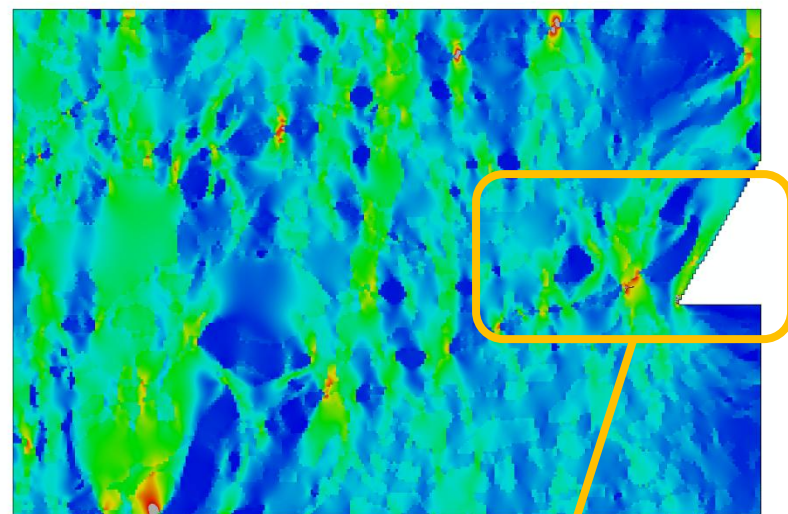
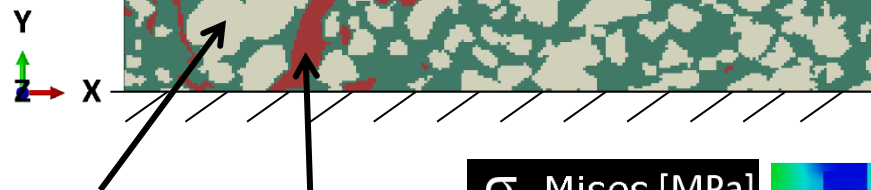


Figure 11

$\epsilon_y = 0.3\%$

FeCrAl matrix

VON MISES STRESS



WC Oxide inclusion

σ , Mises [MPa]
(Avg: 75%)

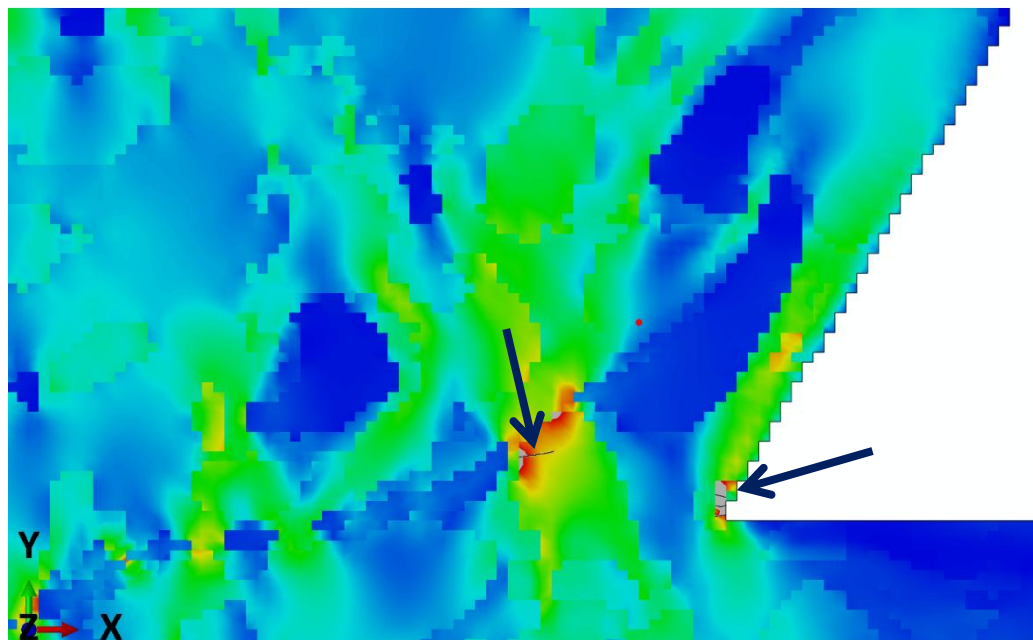
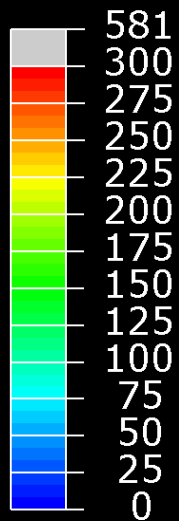
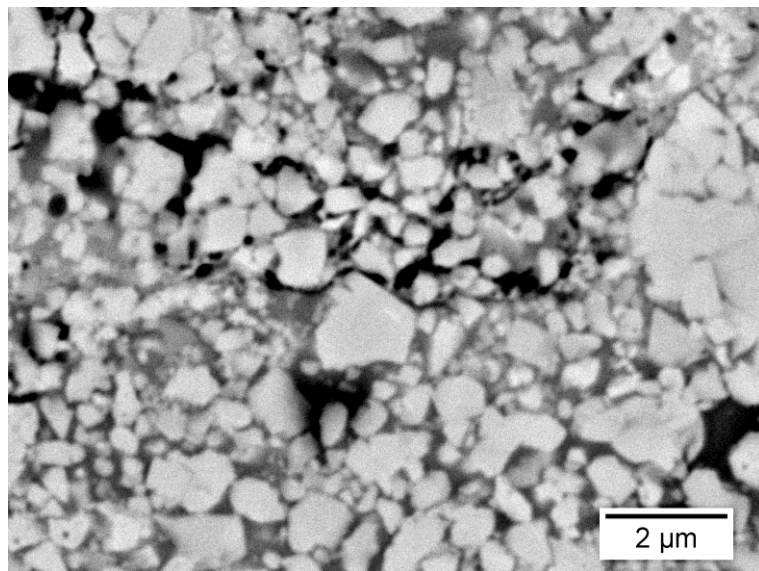
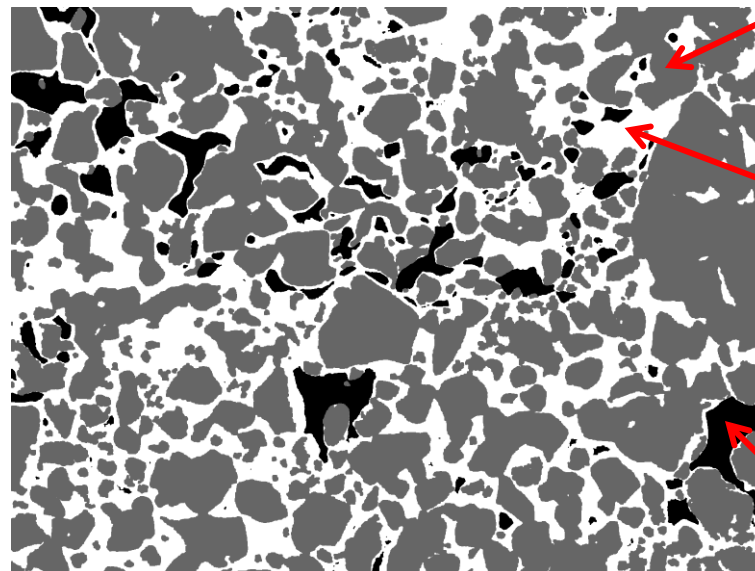


Figure 12

SEM MICROGRAPH



PROCESSED IMAGE

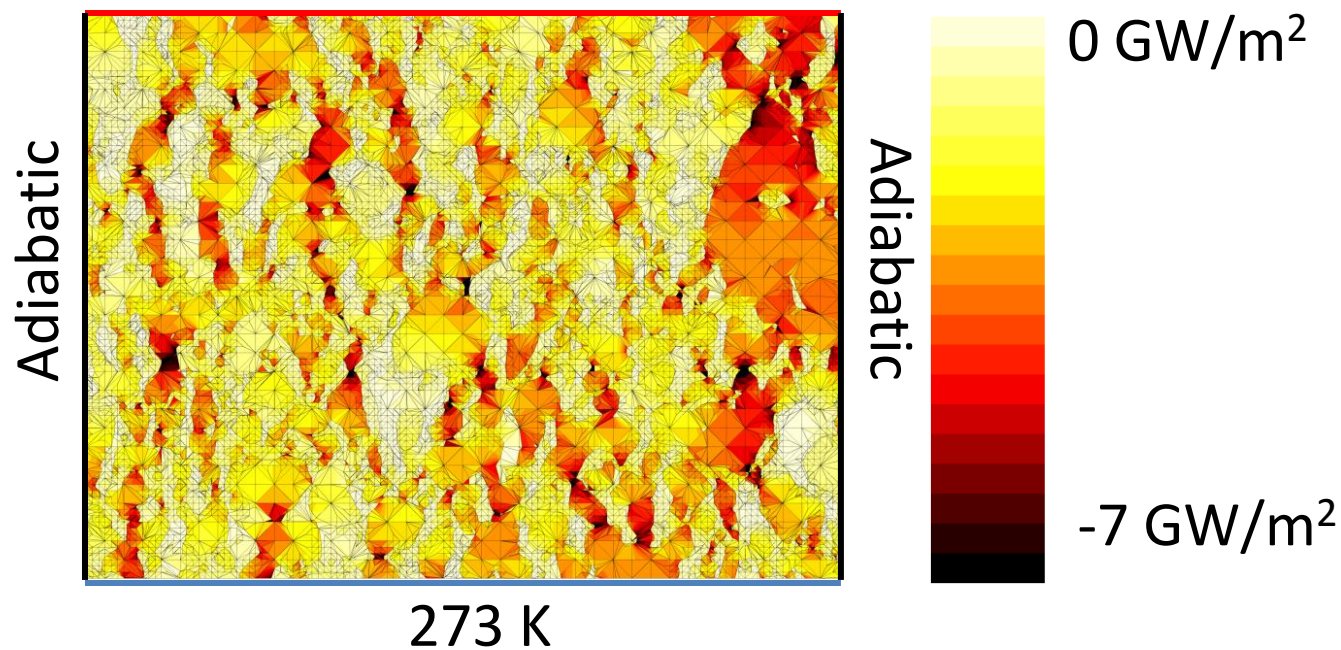


WC

CoCr(W)

Oxide
inclusion

COMPUTED HEAT FLOW
673 K



0 GW/m²

-7 GW/m²

273 K

Figure 13

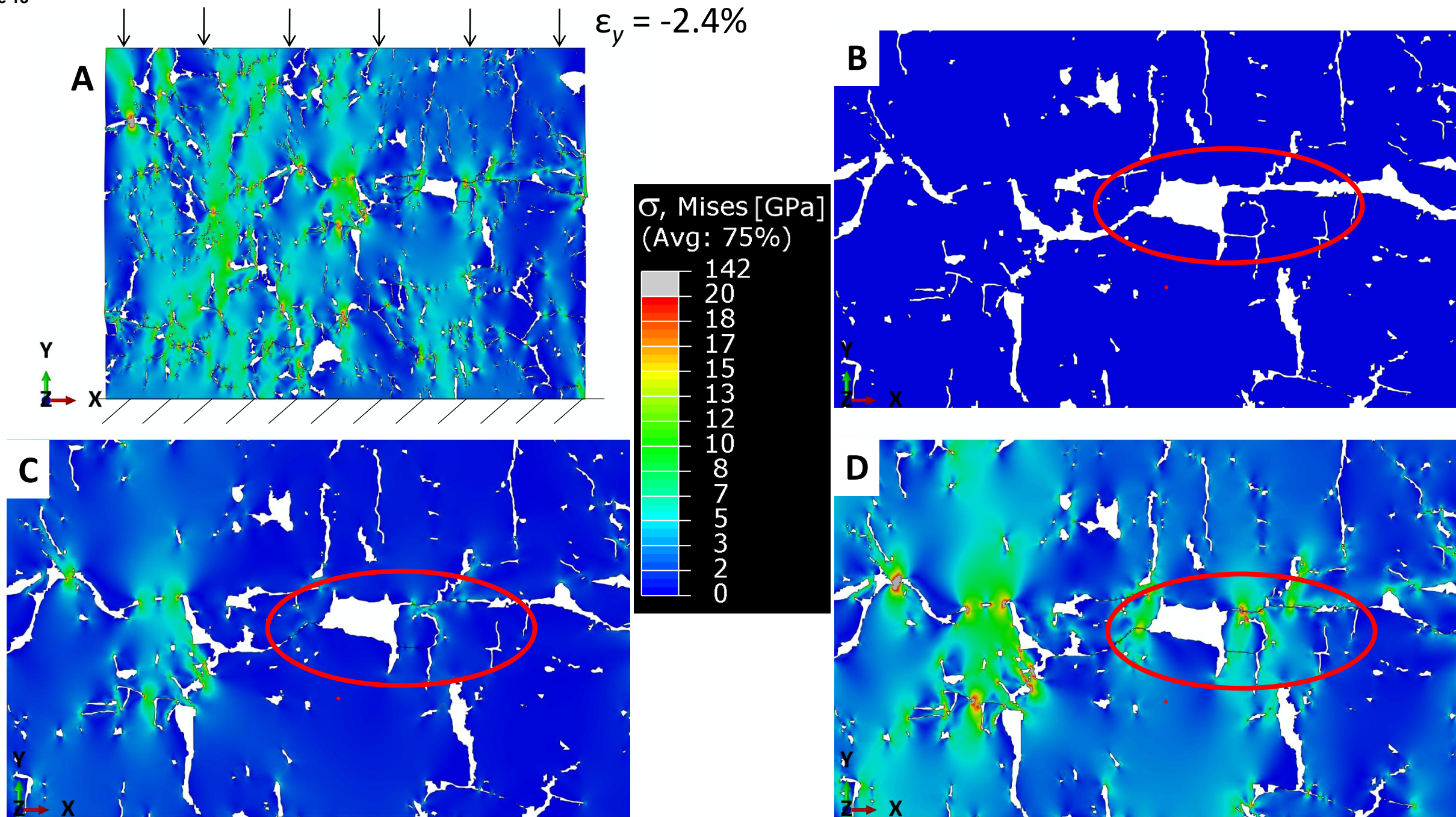


Figure 14

ACCEPTED MANUSCRIPT

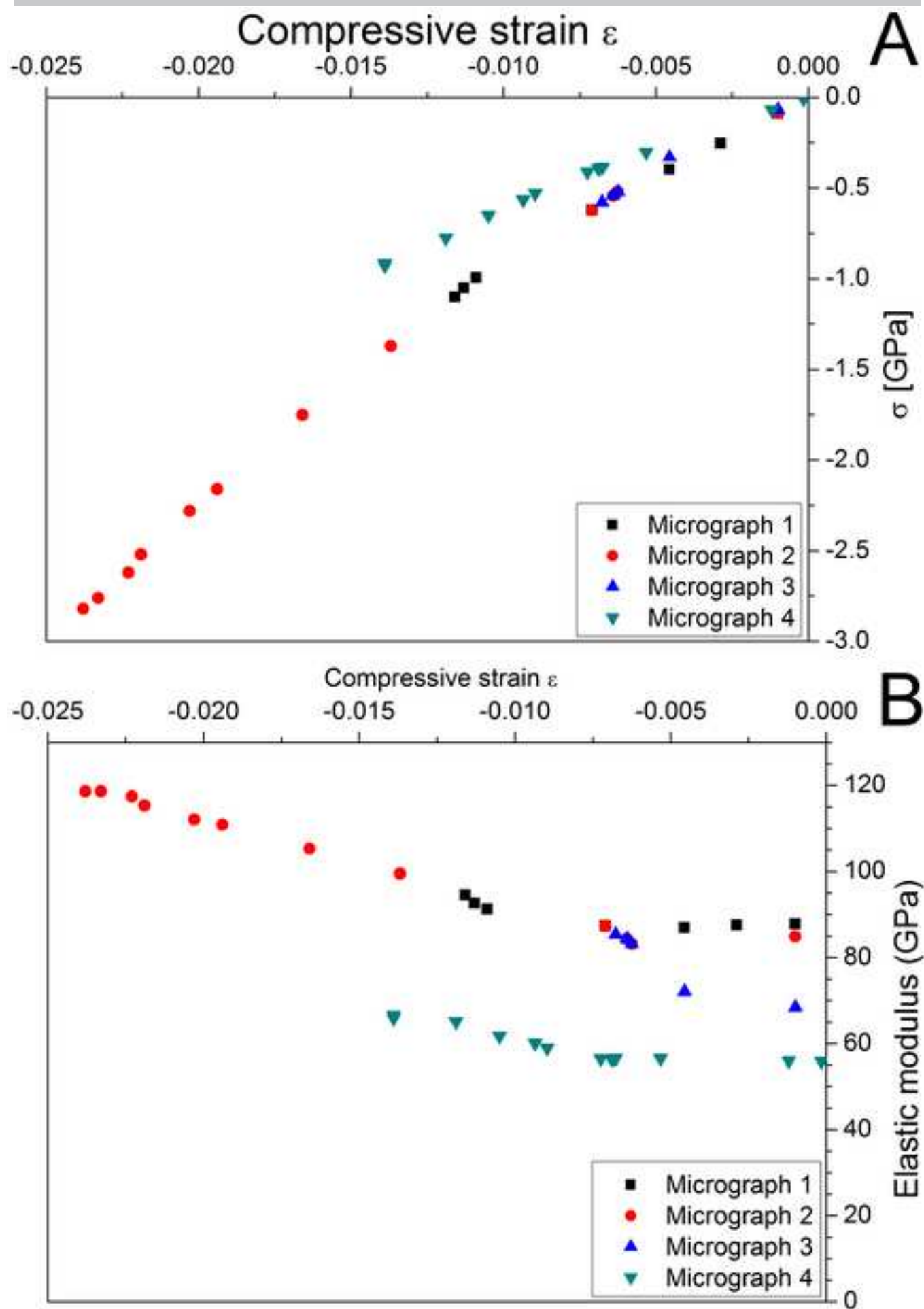


Figure 15

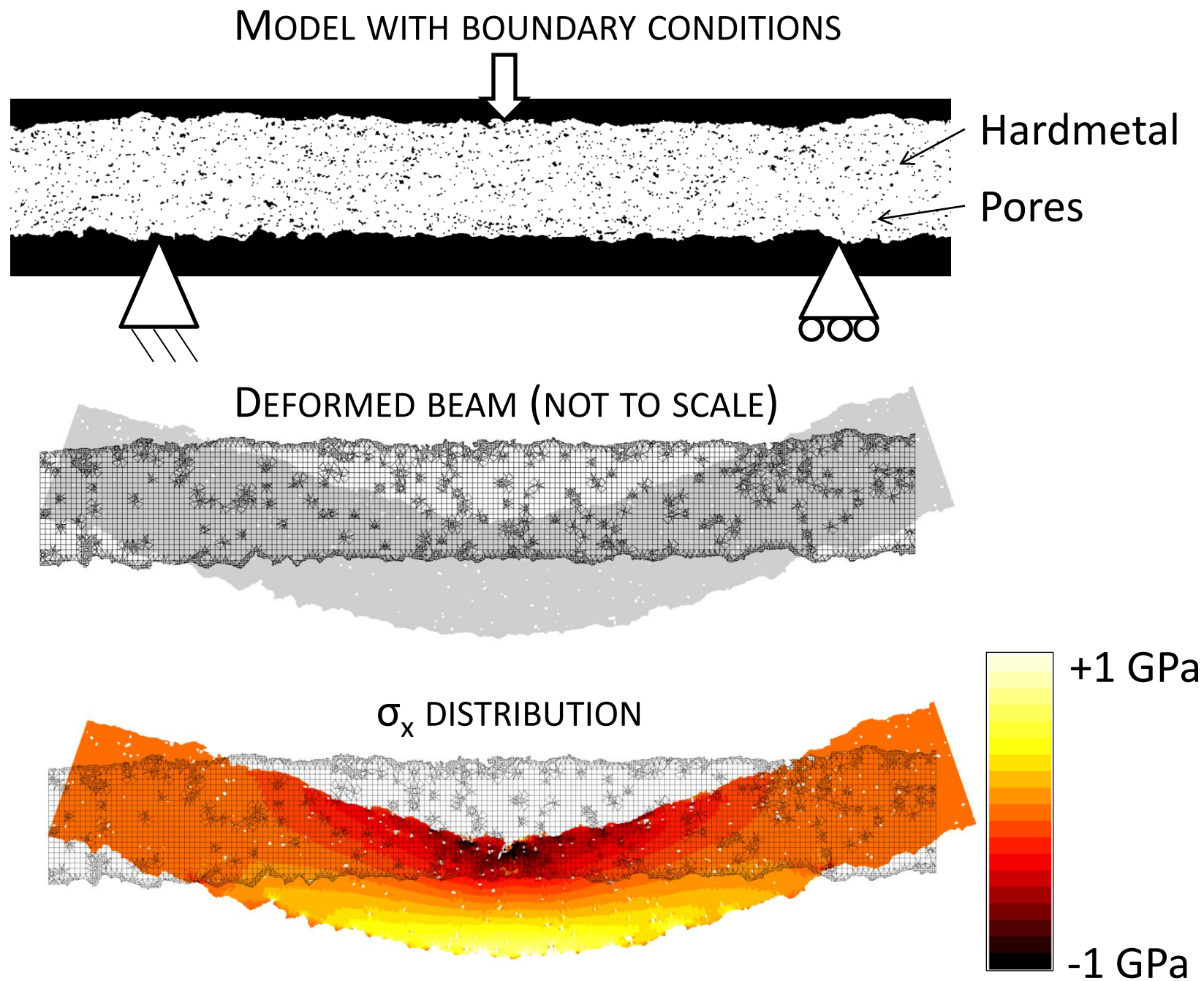
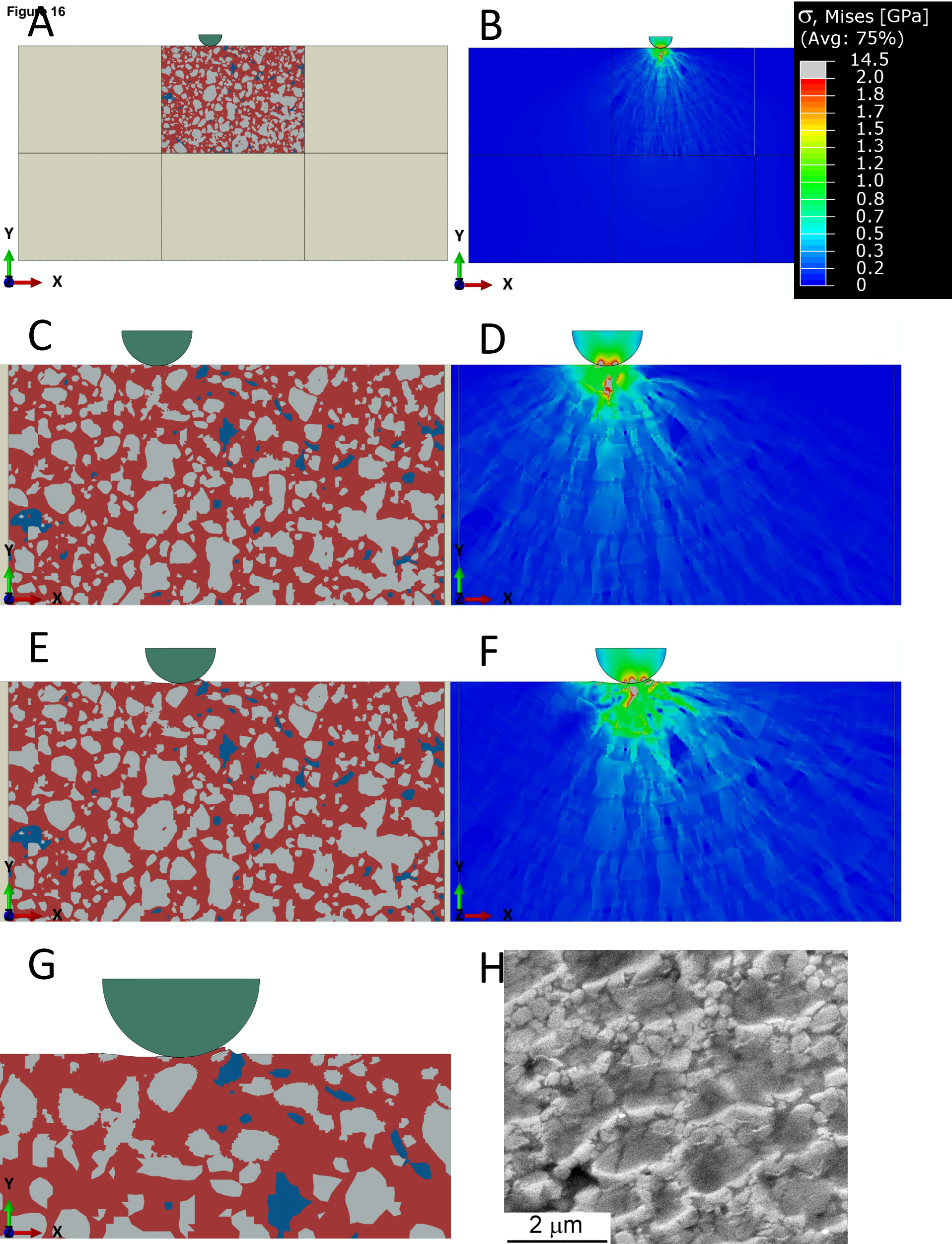
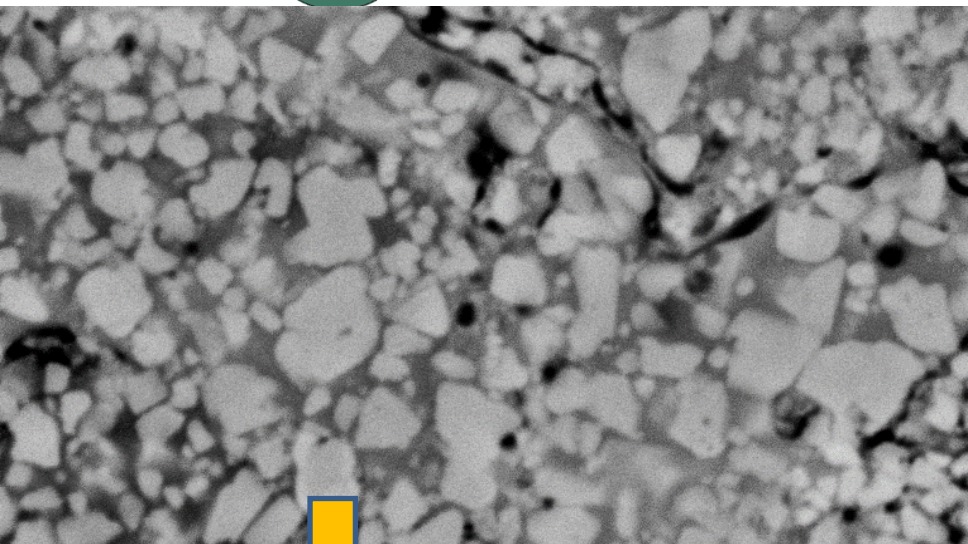


Figure 16



Contact on HVOF WC-CoCr



Von Mises stress [GPa]

